J. Fluid Mech. (2025), *vol*. 1003, A25, doi:10.1017/jfm.2024.1226

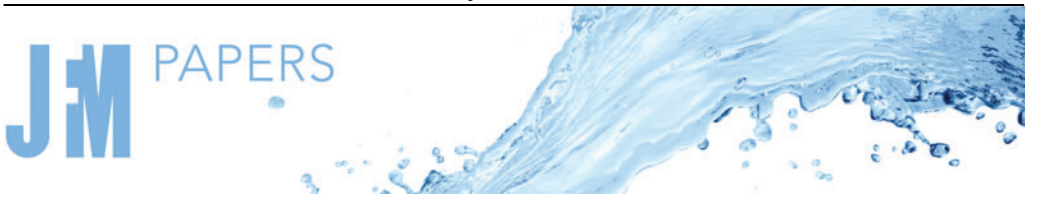

Turbulent kinetic energy budget in compressible turbulent mixing layers: effects of large-scale structures

Xiaoning Wang[1,2,3], **Jing Guo**[1], **Jianchun Wang**[1,2,3,†] **and Shiyi Chen**[1,2,3,4]

[1]Department of Mechanics and Aerospace Engineering, Southern University of Science and Technology, Shenzhen 518055, PR China

[2]Guangdong Provincial Key Laboratory of Turbulence Research and Applications, Southern University of Science and Technology, Shenzhen 518055, PR China

[3]Guangdong-Hong Kong-Macao Joint Laboratory for Data-Driven Fluid Mechanics and Engineering Applications, Southern University of Science and Technology, Shenzhen 518055, PR China

[4]Eastern Institute for Advanced Study, Eastern Institute of Technology, Ningbo 315200, PR China

(Received 23 June 2024; revised 15 December 2024; accepted 17 December 2024)

Direct numerical simulations of temporally developing compressible mixing layers have been performed to investigate the effects of large-scale structures (LSSs) on turbulent kinetic energy (TKE) budgets at convective Mach numbers ranging from $M_c = 0.2$ to 1.8 and at Taylor Reynolds numbers up to 290. In the core region of mixing layers, the volume fraction of low-speed LSSs decreases linearly with respect to the vertical distance at a Mach-number-independent rate. The contributions of low-speed LSSs to TKE, and its budget, including production, dissipation, pressure-strain and spatial diffusion terms, are primarily concentrated in the upper region of mixing layer. The streamwise and vertical mass flux coupling terms mainly transport TKE downwards in low-speed LSSs, and their magnitudes are comparable to the other dominant terms. Near the edges of LSSs, the sources and losses of all three components of TKE are completely different to each other, and dominated by turbulent diffusion, pressure diffusion, pressure-strain and dissipation terms. The TKE, their total variation and dissipation are significantly amplified at edges of low-speed LSSs, especially at the upper edge. This observation supports the existence of amplitude modulation exerted by the LSSs onto the near-edge small-scale structures in mixing layers. The level of amplitude modulation is strongest for the vertical velocity, followed by the streamwise velocity, and weakest for the spanwise velocity. Additionally, the amplitude modulation effect decreases significantly with increasing convective Mach number. The results on the amplitude modulation effect is helpful for developing predictive models of budget terms of TKE in mixing layers.

Key words: compressible turbulence, shear layer turbulence, turbulence simulation

† Email address for correspondence: wangjc@sustech.edu.cn

1. Introduction

Streaky large-scale structures (LSSs) are prevalent in different configurations of shear turbulence, including boundary layers (Hutchins & Marusic 2007; Monty *et al.* 2009; Smits, McKeon & Marusic 2011; Lee, Ahn & Sung 2015; Wang & Zheng 2016; Bross, Scharnowski & Kähler 2021), wakes (Nekkanti *et al.* 2023), jets (Nogueira *et al.* 2019; Samie, Lavoie & Pollard 2021; Samie *et al.* 2022) and mixing (Watanabe *et al.* 2019; Watanabe & Nagata 2021; Wang, Wang & Chen 2022; Wang *et al.* 2024). The high- and low-speed streaky LSSs have been extensively studied in the wall-bounded turbulent flow (Ganapathisubramani *et al.* 2005; Marusic, Mathis & Hutchins 2010; Smits *et al.* 2011; Jiménez 2018), and they have been shown to carry a significant fraction of turbulent kinetic energy and Reynolds shear stress. In wall-bounded turbulent flows, it is now well established that the LSSs interact with the small-scale structures near the wall by means of superposition and amplitude modulation effects (Townsend 1976; Hutchins & Marusic 2007; Mathis, Hutchins & Marusic 2009; Mathis *et al.* 2011*b*; Inoue *et al.* 2012; Liu, Wang & Zheng 2019). Based on the study of amplitude modulation in the smooth-wall boundary layer, Mathis, Hutchins & Marusic (2011*a*) developed a predictive model for the near-wall fluctuations using only a large-scale boundary-layer signal. Yu & Xu (2022) extended this approach to predict near-wall velocity and temperature fluctuations in compressible wall-bounded turbulence. In the turbulent mixing layers, the existence of streamwise elongated high- and low-speed LSSs were confirmed in compressible turbulent mixing layers by Messersmith & Dutton (1996), Pirozzoli *et al.* (2015) and Wang *et al.* (2022), due to the strong stabilizing effects of compressibility. These LSSs highly resemble large-scale turbulent structures identified in wall turbulence.

The transfer of turbulent kinetic energy is crucial to the understanding and modelling of turbulent flows. In a mixing layer, the production and dissipation of turbulent kinetic energy are maximum near the centre and decrease towards the free streams, and the turbulent diffusion transfers turbulent kinetic energy from the middle to the edge of the mixing layer (Rogers & Moser 1994; Pantano & Sarkar 2002). The compressibility effects on the reduced growth rate of mixing layer have been studied through the turbulent energy budgets. With respect to incompressible turbulence, the turbulent kinetic energy transport process in compressible turbulence involves additional terms, including compressible dissipation and pressure-dilatation, which act as sinks exchanging kinetic energy to internal energy. Sarkar (1995) and Vreman, Sandham & Luo (1996) reported that the dilatational contribution to dissipation is negligible even in the present of eddy shocklets, and the compressibility effect of reduced turbulent energy growth rate is primarily due to the reduced level of production and pressure-strain redistribution terms. The direct numerical simulation (DNS) of compressible turbulent mixing layers by Pantano & Sarkar (2002) concluded that production, pressure-strain and transport terms are significantly reduced at high convective Mach number, while the dissipation changes relatively little. Recent numerical studies on compressible mixing layers have shown that the dissipation term decreases with the increasing level of compressibility (Vaghefi 2014; Li *et al.* 2021; Wang *et al.* 2022). Based on an analysis of wave equation for pressure, Pantano & Sarkar (2002) physically explicated that the finite speed of sound in compressible flow introduces a finite time delay in the transmission of pressure signals from one point to an adjacent point, and the resultant increase in decorrelation leads to a reduction in the pressure-strain correlation. The connection between vortex orientation and kinetic energy production has also been investigated. A recent numerical study of mixing layers by Arun *et al.* (2019) showed that the vortical structures at high Mach number tend to align in the streamwise direction, but the tendency is weaker compared with that at low Mach number, which

results in reduced levels of the Reynolds shear stress and suppression of turbulent energy production. They also observed that the orientations of the vortex vectors are less sensitive to compressibility effects with the increase of time. Li *et al.* (2021) examined the energy exchange mechanisms in compressible turbulent mixing layer by analysing the budget terms in transport equations of mean kinetic energy, internal energy and turbulent kinetic energy.

However, the average energy transfer does not reflect what actually happens locally in physical space, between scales and among components. As early as sixty years ago, Lumley (1964) proposed the analysis of spectral budget equations in wall-bounded turbulence to investigate the nonlinear transfer of energy between scales, characterized by the exchange of energy among Fourier modes. This method has been widely used in the study of wall-bounded turbulence (Domaradzki *et al.* 1994; Bolotnov *et al.* 2010; Mizuno 2016; Lee & Moser 2019; Kawata & Tsukahara 2022; Fan & Li 2023), demonstrating the Kolmogorov picture of energy transfer where the kinetic energy is generated at large scales, transferred to hierarchical smaller scales and dissipated finally by viscosity at Kolmogorov length scales. Moreover, the existence of local inverse energy transfers from small to large scales has also been confirmed. Recently, Watanabe & Nagata (2021) performed a spectral analysis of the budget equations using large eddy simulation data of stably stratified mixing layer to investigate large-scale characteristics. They observed similar behaviours of the production, pressure-strain correlation and interscale energy transfer terms to those in channel flows, indicating similar dynamics of the elongated LSSs in the stratified shear layer and wall-bounded shear flows. They confirmed that the LSSs have a negligible contribution to the dissipation of turbulent kinetic energy.

To the best of the authors' knowledge, there is rare analysis of the influence of LSSs on turbulent kinetic energy budgets in physical space, particularly for compressible turbulence. The inhomogeneity of mean shear leads to the spatial inhomogeneity of turbulent kinetic energy budgets (Pope 2000). The generation and distribution of small-scale structures are highly non-uniform. In wall turbulence, a large proportion of small-scale structures reside in the near-wall region or in the near vicinity of edges of uniform momentum zones, while they are sparse within the uniform momentum zones (Adrian, Meinhart & Tonkins 2000; Eisma *et al.* 2015; De Silva *et al.* 2017). The amplitude modulation effect can well demonstrate the spatial inhomogeneity of small-scale structures, showing that the amplitude of the small-scale fluctuations increases beneath the high-speed LSS and decreases above the high-speed LSS (Marusic *et al.* 2010; Mathis *et al.* 2011*a*; Agostini & Leschziner 2014). In compressible turbulent mixing layers, the small-scale vortical structures have an apparent preference for clustering near the top of the large-scale low-speed regions, which is directly associated with high-shearing motions near the upper portion of the low-speed structures (Wang *et al.* 2022, 2024). The modulation scenario in compressible mixing layers bears some similarity to that observed in the outer region of wall-bounded turbulence (Bandyopadhyay & Hussain 1984; Fiscaletti, Ganapathisubramani & Elsinga 2015; Wang *et al.* 2022). Lee *et al.* (2015) observed that the amplitude modulation effect causes high-speed LSSs to have greater intensities than low-speed LSSs near the wall, and *vice versa* in the outer region. Since structures of different scales have varying effects on the turbulent kinetic energy budget, the non-uniform distribution of turbulent structures will result in a non-uniform distribution of the budget terms. The inhomogeneous distribution of small-scale structures inevitably results in the inhomogeneous distribution of viscous dissipation. In other words, LSSs indirectly influence the spatial distribution of dissipation. However, the detailed

mechanism for the impact of the amplitude modulation effect on the turbulent kinetic energy budget remains unknown.

The goal of this paper is to investigate the impact of LSSs on the turbulent kinetic energy budgets in physical space for a compressible turbulent mixing layer, and to further clarify the growth suppression mechanism associated with compressibility effects. The paper is organized as follows. The governing equations and computational method are provided in §§ 2 and 3. In § 4, the main results of the investigation on turbulent kinetic energy budget are presented. Finally, conclusions are drawn in § 5.

2. Direct numerical simulation of compressible mixing layers

We study compressible temporally evolving mixing layer of an ideal gas governed by the following dimensionless Navier–Stokes equations in the conservative form (Wang *et al.* 2012, 2022):

$$\frac{\partial \rho}{\partial t} + \frac{\partial (\rho u_k)}{\partial x_k} = 0, \tag{2.1}$$

$$\frac{\partial (\rho u_i)}{\partial t} + \frac{\partial (\rho u_k u_i)}{\partial x_k} = -\frac{\partial p}{\partial x_i} + \frac{1}{Re}\frac{\partial \sigma_{ik}}{\partial x_k}, \tag{2.2}$$

$$\frac{\partial E}{\partial t} + \frac{\partial [(E+p)u_j]}{\partial x_j} = \frac{1}{\alpha}\frac{\partial}{\partial x_k}\left(\kappa \frac{\partial T}{\partial x_k}\right) + \frac{1}{Re}\frac{\partial (u_j \sigma_{jk})}{\partial x_k}, \tag{2.3}$$

$$p = \rho T/(\gamma M^2), \tag{2.4}$$

where u_i, ρ, p and T are the instantaneous velocity component, density, pressure and temperature, respectively. Here, the viscous stress σ_{ik} is defined as

$$\sigma_{ik} = 2\mu \mathcal{S}_{ik} - \frac{2\mu \Theta}{3}\delta_{ik}, \tag{2.5}$$

in which $\mathcal{S}_{ik} = (\partial u_i/\partial x_k + \partial u_k/\partial x_i)/2$ is the strain rate tensor and $\Theta = \partial u_k/\partial x_k$ is the velocity divergence or dilatation. The total energy per unit volume E is given by

$$E = \frac{p}{\gamma - 1} + \frac{1}{2}\rho u_i u_i. \tag{2.6}$$

Moreover, the temperature-dependent viscosity coefficient μ and thermal conductivity coefficient κ are specified by Sutherland's law (Sutherland 1893).

The variables in the governing equations of compressible turbulence have already been normalized by a set of reference scales, including the reference length L_r, velocity U_r, density ρ_r, pressure $p_r = \rho_r U_r^2$, temperature T_r, energy per unit volume $\rho_r U_r^2$, viscosity μ_r and thermal conductivity κ_r (Samtaney, Pullin & Kosović 2001; Wang *et al.* 2012). There are three reference governing parameters: the reference Reynolds number $Re = \rho_r U_r L_r/\mu_r$, the reference Mach number $M = U_r/c_r$ and the reference Prandtl number $Pr = \mu_r C_p/\kappa_r$, which is assumed to be equal to 0.7. In addition, the reference speed of sound is defined by $c_r = \sqrt{\gamma R T_r}$, where R is the specific gas constant. Here, $\gamma = C_p/C_v$ is the ratio of specific heat at constant pressure C_p to that at constant volume C_v, which is assumed to be equal to 1.4. The parameter α is defined as $\alpha = PrRe(\gamma - 1)M^2$.

A hybrid compact-weighted essentially non-oscillatory (WENO) scheme (Wang *et al.* 2010) is applied for numerical simulations of compressible temporally evolving mixing layer. The hybrid scheme combines an eighth-order compact finite difference

scheme (Lele 1992) in smooth regions and a seventh-order WENO scheme (Balsara & Shu 2000) in shock regions. The numerical simulations essentially resolve flow fields above the Kolmogorov length scale, while the discontinuities around shock waves are captured by the WENO scheme. The computational domain with lengths $L_x \times L_y \times L_z = 314\delta_\theta^0 \times 314\delta_\theta^0 \times 157\delta_\theta^0$ in the streamwise, vertical and spanwise directions is discretized uniformly with the number of grid points equal to $N_x \times N_y \times N_z = 1024 \times 1024 \times 512$, where δ_θ^0 is the initial momentum thickness. The momentum thickness δ_θ is computed by (Vreman *et al.* 1996)

$$\delta_\theta = \frac{1}{\rho_\infty \Delta U^2} \int_{-\infty}^{+\infty} \bar{\rho}\,(\Delta U/2 - \tilde{u})\,(\Delta U/2 + \tilde{u})\ \mathrm{d}y, \tag{2.7}$$

where $\tilde{u}$ and $\bar{\rho}$ are the Favre average of streamwise velocity and the Reynolds average of density, respectively. Here, ΔU is the free stream velocity difference across the shear layer. The Reynolds average of a variable ϕ is denoted by $\bar{\phi}$, while the Reynolds fluctuation is denoted as $\phi' = \phi - \bar{\phi}$. The Favre average of a variable ϕ is denoted by $\tilde{\phi} = \overline{\rho\phi}/\bar{\rho}$, and its Favre fluctuation is denoted as $\phi'' = \phi - \tilde{\phi}$.

Boundary conditions are periodic in the homogeneous streamwise and spanwise directions. To allow periodic configuration in the vertical direction, the mean streamwise velocity is initialized by a hyperbolic tangent profile with two shear layers (one is located at the middle and the other at the boundary of transverse direction),

$$\tilde{u} = \frac{1}{2}\Delta U \left[\tanh\left(\frac{y}{2C_\delta \delta_\theta^0}\right) - \tanh\left(\frac{y + L_y/2}{2C_\delta \delta_\theta^0}\right) - \tanh\left(\frac{y - L_y/2}{2C_\delta \delta_\theta^0}\right) \right], \tag{2.8}$$

where C_δ is an adjustment constant that is determined by the initial momentum thickness δ_θ^0 (Vaghefi 2014; Vaghefi & Madnia 2015; Wang *et al.* 2022). A numerical diffusion zone is applied near the vertical boundary, which can reduce the intensity of possible disturbances at the vertical boundary such that there is a negligible effect on the mixing layer (Reckinger, Livescu & Vasilyev 2016). The mean vertical and spanwise velocities are set to zero. The initial temperature $\mathcal{T}$ is obtained from the Busemann–Crocco relationship (Ragab & Wu 1989; Arun *et al.* 2019) for compressible shear layers,

$$\mathcal{T} = 1 + \tfrac{1}{2}(\gamma - 1)M_c^2(1 - \tilde{u}^2). \tag{2.9}$$

In this equation, the convective Mach number M_c is defined as $M_c = \Delta U/(2c_\infty)$, where c_∞ is the speed of sound in the free stream. The pressure field is uniform and the density field is acquired from the ideal gas equation of state. To accelerate the transition to turbulence, a spatially correlated perturbation velocity field obtained by the digital filter method (Klein, Sadiki & Janicka 2003) is superposed on mean velocities. The filtering length is chosen as the initial vorticity thickness, computed by $\delta_\omega = \Delta U/(\mathrm{d}\tilde{u}/\mathrm{d}y)_{max}$, in each direction.

Several key non-dimensional flow parameters corresponding to the self-similar period at the centreline are presented in table 1. The statistics are obtained by averaging along the homogeneous x and z directions, and in time at normalized time intervals of 25 in the self-similar period. To enhance statistical stability, ensemble averaging was performed over five independent runs with different initial random perturbation for each convective Mach number.

Case	M_c	τ	M_t	Re_θ	Re_λ	Re_ω	$\delta_\theta/\delta_\omega$	Θ_{rms}	ω_{rms}	$\eta/\Delta x$	l_x/L_x	l_z/L_z
M02	0.2	$\tau_0 = 625$	0.10	3768	266	19960	0.189	0.014	11.575	0.42	0.061	0.029
		$\tau_f = 875$	0.09	4798	292	25166	0.191	0.013	12.414	0.46	0.070	0.035
M08	0.8	$\tau_0 = 750$	0.34	2990	202	17230	0.176	0.158	9.771	0.49	0.079	0.021
		$\tau_f = 1250$	0.31	4546	236	26028	0.175	0.150	10.858	0.56	0.123	0.025
M18	1.8	$\tau_0 = 1250$	0.65	3036	200	21158	0.142	1.027	7.867	0.86	0.090	0.036
		$\tau_f = 2250$	0.57	5232	234	38094	0.136	0.906	9.292	1.05	0.151	0.043

Table 1. Simulation parameters at the beginning ($\tau = \tau_0$) and end ($\tau = \tau_f$) of the self-similar period. The values of M_t, Re_λ, K, ω, Θ_{rms}, η, l_x and l_z are obtained at $y = 0$.

The numerical simulations have been performed for three different convective Mach numbers, $M_c = 0.2, 0.8, 1.8$. The Reynolds numbers based on the momentum thickness Re_θ, the vorticity thickness Re_ω and the Taylor microscale Re_λ are defined as

$$Re_\theta = \frac{\rho_\infty \Delta U \delta_\theta}{\mu_\infty}, \quad Re_\omega = \frac{\rho_\infty \Delta U \delta_\omega}{\mu_\infty}, \quad Re_\lambda = 2K\sqrt{\frac{5\rho}{\mu\epsilon}}, \tag{2.10a–c}$$

respectively, where ϵ is the turbulent kinetic energy dissipation rate per unit mass and μ is the viscosity coefficient. The initial momentum thickness Reynolds number is $Re_\theta = 320$. The self-similar period is carefully determined by analysing the time evolution of the mean velocity, Reynolds stresses and integrated transfer terms of turbulent kinetic energy. The resulting time duration of the self-similar period is from τ_0 to τ_f. The turbulent Mach number $M_t = \sqrt{2K}/c$ ranges from 0.1 to 0.6, where K is the turbulent kinetic energy and c is the average speed of sound. The lowest turbulent Mach number case corresponds to a nearly incompressible condition, while the highest turbulent Mach number case almost approaches the strongest compressibility effects reported in the literature of numerical simulations (Pantano & Sarkar 2002; Arun *et al.* 2019; Wang *et al.* 2022), to the best of our knowledge.

The integral length scales in the streamwise direction (l_x) and spanwise direction (l_z) are defined as

$$l_x = \int_0^{L_x/2} \mathcal{R}_{xu}(r_x)\,\mathrm{d}r_x, \quad l_z = \int_0^{L_z/2} \mathcal{R}_{zu}(r_z)\,\mathrm{d}r_z, \tag{2.11a,b}$$

respectively. Here, $\mathcal{R}_{xf}$ and $\mathcal{R}_{zf}$ are the two-point correlation of a variable f in streamwise and spanwise directions, respectively. They are defined as

$$\mathcal{R}_{xf}(r_x) = \frac{\langle f'(x,0,z) f'(x+r_x,0,z)\rangle}{f_{rms}^2}, \quad \mathcal{R}_{zf}(r_z) = \frac{\langle f'(x,0,z) f'(x,0,z+r_z)\rangle}{f_{rms}^2}, \tag{2.12a,b}$$

where $\langle\rangle$ stands for ensemble average. The integral length scales in the streamwise and spanwise directions are sufficiently small compared with the length of the computational domain, ensuring that the self-similar growth of LSSs is not confined. Additional discussions on the confinement effects of the computational domain are provided in the Appendix. In terms of the local Kolmogorov length scale $\eta = (\mu^3/(\rho^3\epsilon))^{1/4}$, the resolution parameter $\eta/\Delta x$ is in the range $0.42 \leq \eta/\Delta x \leq 1.05$ at the centreline, where Δx is the grid length in each direction, indicating that the resolution of the present simulations is fine enough to resolve the smallest scales in the flow, as given in table 1. A detailed

description and a comprehensive validation of the DNS can be found in recent works by the authors (Wang *et al.* 2022, 2024).

3. Budget equations for turbulent kinetic energy

The non-dimensional form of the fluctuating velocity field equation for a compressible temporally evolving mixing layer can be written as (Arun *et al.* 2021)

$$\frac{\partial \rho u_i''}{\partial t} + \frac{\partial \rho u_i'' u_j}{\partial x_j} + \rho u_j'' \frac{\partial \tilde{u}_i}{\partial x_j} = \frac{\rho}{\bar{\rho}} \frac{\partial \overline{\rho u_i'' u_j''}}{\partial x_j} - \frac{\partial p' \delta_{ij}}{\partial x_j} + \frac{1}{Re} \frac{\partial \sigma_{ij}'}{\partial x_j} + \left(1 - \frac{\rho}{\bar{\rho}}\right) \left(-\frac{\partial \bar{p} \delta_{ij}}{\partial x_j} + \frac{1}{Re} \frac{\partial \bar{\sigma}_{ij}}{\partial x_j}\right). \tag{3.1}$$

By multiplying (3.1) with u_i'', the budget equation for instantaneous turbulent kinetic energy, $K = (\rho u_i'' u_i'')/2$, is obtained as follows:

$$\frac{\partial K}{\partial t} + \frac{\partial K \tilde{u}_k}{\partial x_k} = T + P + \Phi - \epsilon + \Sigma. \tag{3.2}$$

Here, the left-hand side two terms represent the temporal variation term and the convective term, respectively. Their sum represents the total variation of turbulent kinetic energy as moving with a fluid element, which will be denoted as V in the following. Here, T is the spacial diffusion of turbulent kinetic energy, P is the production term, Φ is the pressure-dilatation term, ϵ is the viscous dissipation term and Σ is the mass flux coupling term. These terms are defined as

$$T = T_t + T_p + T_v, \tag{3.3a}$$

$$T_t = -\frac{1}{2} \frac{\partial \rho u_i'' u_i'' u_k''}{\partial x_k}, \quad T_p = -\frac{\partial p' u_i'' \delta_{ik}}{\partial x_k}, \quad T_v = \frac{1}{Re} \frac{\partial \sigma_{ik}' u_i''}{\partial x_k}, \tag{3.3b}$$

$$P = -\rho u_i'' u_k'' \frac{\partial \tilde{u}_i}{\partial x_k}, \tag{3.3c}$$

$$\Phi = p' \frac{\partial u_i''}{\partial x_i}, \tag{3.3d}$$

$$\epsilon = \frac{1}{Re} \sigma_{ik}' \frac{\partial u_i''}{\partial x_k}, \tag{3.3e}$$

$$\Sigma = \frac{\rho u_i''}{\bar{\rho}} \frac{\partial \overline{\rho u_i'' u_k''}}{\partial x_k} + u_i'' \left(1 - \frac{\rho}{\bar{\rho}}\right) \left(\frac{1}{Re} \frac{\partial \bar{\sigma}_{ik}}{\partial x_k} - \frac{\partial \bar{p}}{\partial x_i}\right), \tag{3.3f}$$

where the total diffusion T includes turbulent diffusion T_t, pressure diffusion T_p (pressure–velocity interaction) and viscous diffusion T_v. Among the above terms, the diffusion, production and dissipation terms are dominant in the transport of turbulent kinetic energy K. The mass flux coupling term is negligibly small after ensemble averaging (Pantano & Sarkar 2002), but it becomes comparable to the other dominant terms when conditional averaging is applied, as will be shown in the subsequent analysis of this paper. The transport equation for the turbulent kinetic energy components K_i can be simply obtained by avoiding summation convention over repeated indices i in (3.2) and (3.3), and the corresponding transport terms are V_i, T_i, P_i, Φ_i, ϵ_i and Σ_i (Pantano & Sarkar 2002; Arun *et al.* 2019). The pressure-strain term, Φ_i, becomes dominant for redistributing energy between three components of turbulent kinetic energy.

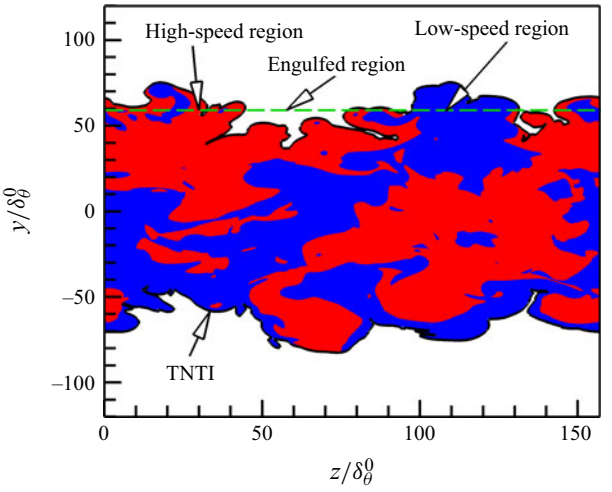

Figure 1. An example of high-speed LSSs (red contours of $u'' > 0$) and low-speed LSSs (blue contours of $u'' < 0$) in fluctuating streamwise velocity field is shown in the y–z plane. The black solid lines present the TNTI. The green dashed line show a specific horizontal plane.

4. Results and discussions on turbulent kinetic energy budget

The high- and low-speed LSSs can be detected by the premultiplied energy spectra (Kim & Adrian 1999; Monty *et al.* 2009; Watanabe & Nagata 2021), the two-point correlation of fluctuating streamwise velocity (Ganapathisubramani *et al.* 2005; Monty *et al.* 2007; Wang *et al.* 2022) or the proper orthogonal decomposition (Baltzer, Adrian & Wu 2013; Pirozzoli *et al.* 2015). In the instantaneous flow field, individual high- and low-speed LSSs are usually extracted by the isosurfaces of the fluctuating streamwise velocity that exceed a threshold value (Dennis & Nickels 2011; Lee *et al.* 2014; Deng *et al.* 2018). In this paper, we set the threshold value to zero, meaning that the turbulent region consists only of low-speed LSSs with $u'' < 0$ and high-speed LSSs with $u'' > 0$. Unlike Lee *et al.* (2015), we did not apply filtering to the flow field, which means the LSSs in the instantaneous field include both large-scale turbulent structures and embedded small-scale turbulent structures. This approach allows us to analyse the influence of LSSs on the spatial distribution of turbulent kinetic energy transport terms, as well as the multiscale characteristics of turbulence. The turbulent/non-turbulent interface (TNTI) is used as the outer edge of LSSs instead of the outer parts of the contour lines of $u''/\Delta U = 0$, similar to the outer edge of the uniform momentum zones (De Silva *et al.* 2017; Fan *et al.* 2019). In figure 1, the high- and low-speed LSSs in fluctuating streamwise velocity field is shown in the y–z plane for example. An isoline of the root-mean-square (r.m.s.) vorticity magnitude $\omega_{rms} = 0.01\Delta U/\delta_\theta^0$ is selected as the nominal threshold to identify the TNTI (Jahanbakhshi & Madnia 2016; Watanabe, Zhang & Nagata 2018; Wang *et al.* 2022).

At each horizontal plane, the instantaneous field of mixing layers is classified into three groups: low-speed regions with $u'' < 0$, high-speed regions with $u'' > 0$ and engulfed regions, as shown in figure 1. The engulfed region refers to the non-turbulent area induced by the rollup of LSSs. According to this classification, the Reynolds average of physical quantity ϕ can be decomposed into three parts as

$$\bar{\phi} = \bar{\phi}_n + \bar{\phi}_p + \bar{\phi}_e, \tag{4.1}$$

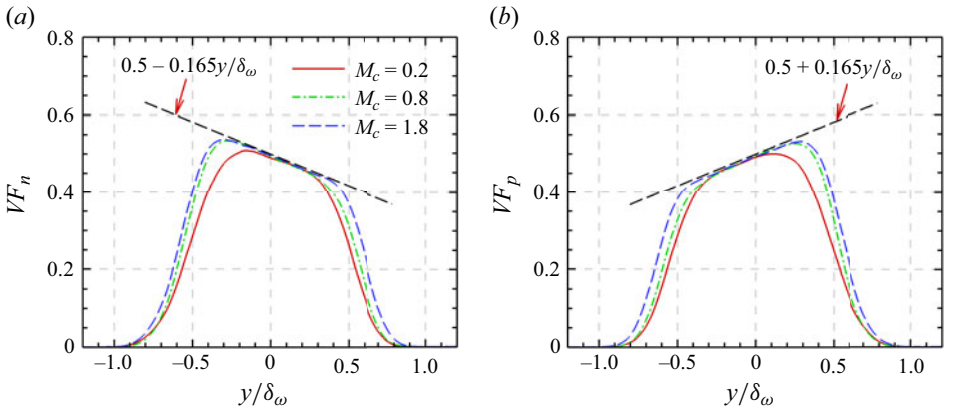

Figure 2. Volume fraction of (*a*) low-speed LSS and (*b*) high-speed LSS at $M_c = 0.2$, 0.8 and 1.8.

where the three terms on the right-hand side represent contributions of the low-speed LSSs, high-speed LSSs and engulfed regions to $\bar{\phi}$ (denoted by subscripts n, p and e, respectively). The contribution of the engulfed regions or non-turbulent flow is negligibly small and will not be discussed in the following.

To study the influence of LSSs on the spatial distribution of a physical quantity, we apply conditional average method based on the magnitude of u'' in the turbulent region. The conditionally averaged physical quantity $\phi(x, y, z, t)$ based on the low-speed LSSs can subsequently be defined as

$$\hat{\phi}_n(y) = \langle \phi(x, y, z, t) | u''(x, y, z, t) < 0, TR \rangle, \tag{4.2}$$

where TR indicates that the conditioning point is located in turbulent regions, and the subscript n donates in regions with negative u''. The two-dimensional conditionally averaged physical quantity $\phi(x, y, z, t)$ based on the condition of $u'' < -0.15\Delta U$ is defined as

$$\breve{\phi}_n(r_x, r_y) = \langle \phi(x + r_x, y + r_y, z, t) | u''(x, y, z, t) < -0.15\Delta U, TR \rangle, \tag{4.3}$$

where r_x and r_y represent the streamwise and vertical distances from the conditioning point, respectively. Only strong-u'' regions within low-speed LSSs are chosen.

Figure 2(*a*) presents the volume fraction of low-speed LSSs (VF_n) as a function of the vertical distance y/δ_ω at convective Mach numbers $M_c = 0.2$, 0.8 and 1.8. In the core region of the mixing layer, VF_n decreases linearly with respect to the vertical distance at a coefficient of 0.165 ($VF_n = 0.5 - 0.165y/\delta_\omega$). As the convective Mach number increases, the linear region of VF_n extends over a broader range, but the coefficient remains nearly constant. Beyond this linear decrease region, VF_n rapidly decreases towards the mixing layer edges and approaches almost zero when $y/\delta_\omega < -1.0$ or $y/\delta_\omega > 0.9$. This occurs because of the increased intermittency effects at the edge of the mixing layer, which means that the proportion of non-turbulent flow rapidly increases (Watanabe *et al.* 2019). Note that the volume fraction of the high-speed LSSs VF_p exhibits a very good symmetry with respect to VF_n in the mixing layer. Due to the symmetry of high- and low-speed LSSs in temporally developing mixing layers, the statistics related to high-speed LSSs are omitted for brevity in the following analysis. The non-uniform distribution of volume fraction of low-speed LSSs can significantly influence the contribution of LSSs to turbulent kinetic energy and its transport processes.

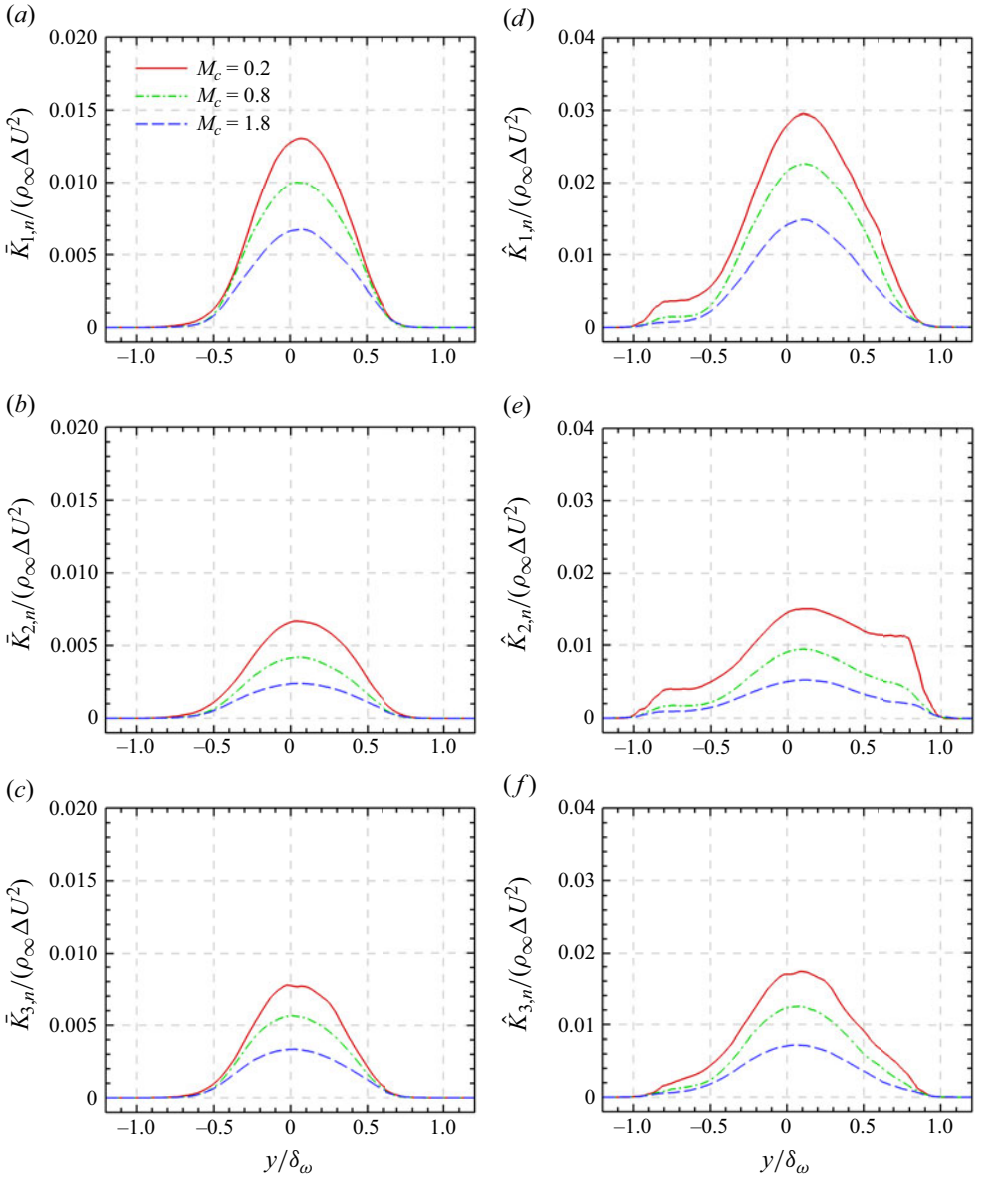

Figure 3. (*a–c*) Contributions of the low-speed LSSs to turbulent kinetic energy $\bar{K}_{i,n}/(\rho_\infty \Delta U^2)$ and (*d–f*) conditionally averaged turbulent kinetic energy $\hat{K}_{i,n}/(\rho_\infty \Delta U^2)$ at $M_c = 0.2$, 0.8 and 1.8. (*a*,*d*) Streamwise, (*b*,*e*) vertical and (*c*,*f*) spanwise components.

4.1. *Turbulent kinetic energy*

Figures 3(*a*)–3(*c*) present the contributions of the low-speed LSSs to the turbulent kinetic energy $\bar{K}_{i,n}/(\rho_\infty \Delta U^2)$ at convective Mach numbers $M_c = 0.2$, 0.8, 1.8. The components of the turbulent kinetic energy are normalized by $\rho_\infty \Delta U^2$. Previous studies have demonstrated the symmetry of $\bar{K}_i$ about the centre plane of the mixing layers (Rogers & Moser 1994; Pantano & Sarkar 2002; Wang *et al.* 2022). However, figures 3(*a*)–3(*c*) show distinct upward shifts in the peak positions of $\bar{K}_{i,n}/(\rho_\infty \Delta U^2)$, suggesting that the contributions of the low-speed LSSs are dominant in the upper half of the mixing layer.

This observation is qualitatively similar to the results of Lee *et al.* (2015) in wall-bounded turbulence, but the distribution in the vertical direction in wall turbulence is more complex. Lee *et al.* (2015) observed that low-speed LSSs contribute more to turbulent kinetic energy in the outer region, while high-speed LSSs contribute more in the near-wall region. In mixing layers, the low-speed LSSs contribute more to turbulent kinetic energy in the upper half-region, while high-speed LSSs contribute more in the lower half-region.

Figures 3(*d*)–3(*f*) show the conditionally averaged turbulent kinetic energy conditioned on the low-speed LSSs $\hat{K}_{i,n}/(\rho_\infty \Delta U^2)$ at convective Mach numbers $M_c = 0.2,\ 0.8,\ 1.8$. Compared with the profiles of $\bar{K}_{i,n}/(\rho_\infty \Delta U^2)$, the profiles of $\hat{K}_{i,n}/(\rho_\infty \Delta U^2)$ are similar in the central region of the mixing layer, but are significantly amplified at the edges, especially for the streamwise and vertical components of turbulent kinetic energy. At $M_c = 0.2$, $\hat{K}_{2,n}/(\rho_\infty \Delta U^2)$ exhibits two plateaus, located at $-0.8 < y/\delta_\omega < -0.6$ and $0.6 < y/\delta_\omega < 0.8$, respectively. Surprisingly, when $y/\delta_\omega > 0.7$, the vertical turbulent kinetic energy exceeds the streamwise turbulent kinetic energy. As the convective Mach number increases from $M_c = 0.2$ to 1.8, the magnitudes of $\hat{K}_{i,n}/(\rho_\infty \Delta U^2)$ become smaller in both the central region and edges of the mixing layer, demonstrating the significant suppression of compressibility on the turbulent kinetic energy. Interestingly, their peak positions remain insensitive to the convective Mach number.

From the perspective of turbulent structures, the turbulent kinetic energy at the central region of the mixing layer primarily originates from LSSs, while near the edges of the mixing layer, it mainly comes from small-scale structures. The amplification of turbulent kinetic energy near the edges of the mixing layer is consistent with the amplitude modulation effect exerted by the LSSs onto the near-edge small-scale structures. This effect has been extensively studied in wall turbulence (Marusic *et al.* 2010; Mathis *et al.* 2011*a*; Agostini & Leschziner 2014) and has also been confirmed in free shear layers (Bandyopadhyay & Hussain 1984; Fiscaletti *et al.* 2015; Wang *et al.* 2022, 2024), including turbulent wakes, mixing layers and jets. Talluru *et al.* (2014) reported that in wall turbulence, all three components of velocity are modulated in a very similar manner and the amplitude modulation is relatively uniform across all three velocity components. However, according to figures 3(*d*)–3(*f*), the amplitude modulation in the mixing layers is not uniform across all three velocity components. The vertical velocity exhibits stronger amplitude modulation compared with the streamwise and spanwise components, with the spanwise velocity showing the least significant amplitude modulation. Meanwhile, we infer that the degree of amplitude modulation decreases with increasing convective Mach number in compressible mixing layers.

4.2. *Production*

Figure 4(*a*) shows the contribution of low-speed LSSs to the production of turbulent kinetic energy $\bar{P}_n/\bar{\epsilon}_c$ at convective Mach numbers $M_c = 0.2,\ 0.8,\ 1.8$. The budget terms are normalized by the average dissipation at the centreline $\bar{\epsilon}_c$. The production contribution of low-speed LSSs $\bar{P}_n/\bar{\epsilon}_c$ is unimodal with the peak located in the upper half of the mixing layer ($y > 0$). Before reaching the edge of the mixing layer, when $y/\delta_\omega > 0.7$ or $y/\delta_\omega < -0.6$, $\bar{P}_n/\bar{\epsilon}_c$ is nearly zero. This observation highlights that the dominant contribution of the low-speed LSSs to the production comes from the upper half of the mixing layer. Here, $\bar{P}_n/\bar{\epsilon}_c$ for different Mach numbers do not completely overlap, displaying a separation of approximately 10 % to 20 %. For $y/\delta_\omega > -0.25$, the production contribution of low-speed LSSs is highest at $M_c = 0.2$, moderate at $M_c = 1.8$ and lowest at

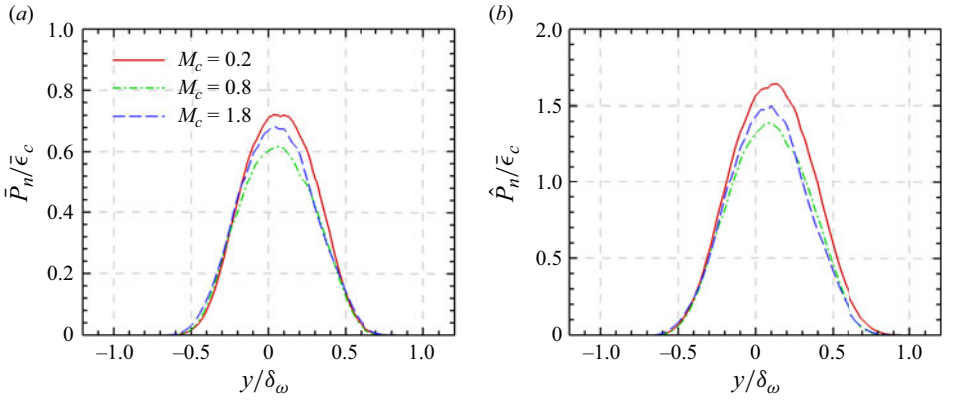

Figure 4. (*a*) Contributions of the low-speed LSSs to production $\bar{P}_n/\bar{\epsilon}_c$ and (*b*) conditionally averaged production $\hat{P}_n/\bar{\epsilon}_c$ based on low-speed events with $u'' < 0$ at $M_c = 0.2$, 0.8 and 1.8.

$M_c = 0.8$, indicating a non-monotonic variation with M_c. Conversely, for $y/\delta_\omega < -0.25$, $\bar{P}_n/\bar{\epsilon}_c$ increases with increasing M_c.

Figure 4(*b*) shows the conditionally averaged production term conditioned on the low-speed LSSs $\hat{P}_n/\bar{\epsilon}_c$ at convective Mach numbers $M_c = 0.2$, 0.8, 1.8. The shapes of $\bar{P}_n/\bar{\epsilon}_c$ and $\hat{P}_n/\bar{\epsilon}_c$ are similar to each other. Unlike $\hat{K}_{i,n}/(\rho_\infty \Delta U^2)$, $\hat{P}_n/\bar{\epsilon}_c$ is not amplified at the edges of the mixing layer, indicating that the small-scale structures hardly generate turbulent kinetic energy. Overall, the production term is highest at $M_c = 0.2$, moderate at $M_c = 1.8$ and lowest at $M_c = 0.8$, indicating a non-monotonic relationship with M_c, except for $0.3 < y/\delta_\omega < 0.6$. When normalized by $\rho\infty\Delta U^3/\delta_\omega$, the production of the TKE $\bar{P}_n$ clearly shows a monotonic decrease with increasing M_c, consistent with previous studies (Pantano & Sarkar 2002; Vaghefi 2014), although this result is not presented in this paper.

Figures 5(*a*) and 5(*b*) show two-dimensional conditionally averaged velocity and production based on the condition of $u'' < -0.15\Delta U$ at convective Mach numbers $M_c = 0.2$ and 1.8. The velocity is normalized by ΔU. The conditionally averaged streamwise velocity $\breve{u}_n/\Delta U$ (solid lines) demonstrates elongated forward-leaning LSSs, extending a distance of $2\delta_\omega$ in the streamwise direction. These structures exhibit a strong negative correlation with the conditionally averaged vertical velocity $\breve{v}_n/\Delta U$ (dashed lines), indicating that low-speed LSSs are predominantly moving upwards. The spatial distribution of the production is inherently similar to the shape of the LSSs, confirming that LSSs contribute favourably to the turbulence production. The production mainly occurs at the centre of the LSSs, and decreases as the convective Mach number increases from $M_c = 0.2$ to 1.8.

We decompose the kinetic energy production P into a positive component P^+ and a negative component P^-: $P = P^+ + P^-$. Here, $P^+ = 0.5(P + |P|)$ and $P^- = 0.5(P - |P|)$. The positive production is contributed by negative Reynolds shear stress corresponding to Q2 and Q4 events (or ejection and sweep events) in quadrant analysis, while the negative production is contributed by positive Reynolds shear stress corresponding to Q1 and Q3 events (or positive quadrant events) (Pope 2000; Wallace 2016). On average, the low-speed LSSs move upwards, and the high-speed LSSs move downwards; namely, they contribute most of the positive kinetic energy production. In figures 5(*c*) and 5(*d*), we present the conditionally averaged negative component of production $\breve{P}_n^-/\bar{\epsilon}_c$, which is significantly smaller than the total production $\breve{P}_n/\bar{\epsilon}_c$. At $M_c = 0.2$, negative production events are

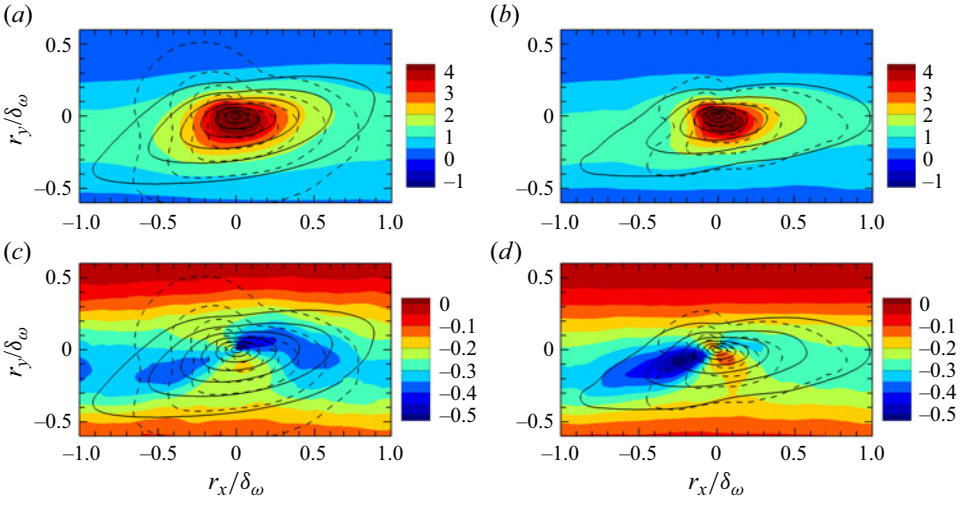

Figure 5. Two-dimensional conditionally averaged production $\breve{P}_n/\bar{\epsilon}_c$ (contours), streamwise velocity $\breve{u}_n/\Delta U$ (solid lines) and vertical velocity $\breve{v}_n/\Delta U$ (dashed lines), and based on low-speed events with $u'' < -0.15\Delta U$ at (*a*) $M_c = 0.2$, (*b*) $M_c = 1.8$. Conditionally averaged negative component of production $\breve{P}_n^-/\bar{\epsilon}_c$ at (*c*) $M_c = 0.2$, (*d*) $M_c = 1.8$.

mainly concentrated within the upper-right region of the low-speed LSSs. Conversely, at $M_c = 1.8$, these negative production events primarily emerge within the lower-left region of the low-speed LSSs.

4.3. *Dissipation*

Figure 6(*a*) shows the contribution of low-speed LSSs to the dissipation of turbulent kinetic energy $\bar{\epsilon}_n/\bar{\epsilon}_c$ at convective Mach numbers $M_c = 0.2$, 0.8, 1.8. The dissipation contribution of low-speed LSS $\bar{\epsilon}_n/\bar{\epsilon}_c$ is unimodal peaking around $y/\delta_\omega \approx 0.1$. This observation indicates that the dissipation induced by low-speed LSSs tends towards the upper portion of the mixing layer. Unlike the contribution of low-speed LSSs to the production term, $\bar{\epsilon}_n/\bar{\epsilon}_c$ remains non-zero near the edge of the mixing layer, extending until $y/\delta_\omega > 0.8$ or $y/\delta_\omega < -0.8$. In the profile of conditionally averaged dissipation $\hat{\epsilon}_n/\bar{\epsilon}_c$, the dissipation near the edge of the mixing layer is significantly amplified, as shown in figure 6(*b*). It is evident that in regions $-1.0 < y/\delta_\omega < -0.5$ and $0.5 < y/\delta_\omega < 1.0$, there are noticeable bumps in $\hat{\epsilon}_n/\bar{\epsilon}_c$, with the bump being more prominent in the upper region. This observation confirms that the amplification of turbulent kinetic energy near the edges of the mixing layer is due to small-scale structures, as shown in figures 3(*d*)–3(*f*). As the convective Mach number increases, these bumps of $\hat{\epsilon}_n/\bar{\epsilon}_c$ rapidly decrease but still persist.

When normalized by $\rho_\infty \Delta U^3/\delta_\omega$, the dissipation decreases rapidly with increasing convective Mach number, as shown in figure 6(*c*). This trend is in good agreement with previous results reported by Vaghefi (2014). However, Pantano & Sarkar (2002) reported that the dissipation changes relatively little with varying convective Mach numbers. The error bar in figure 6(*a*) represents the discrepancy between the streamwise and vertical dissipation components, with each representing the maximum and minimum dissipation component, respectively. It is clear to see that the dissipation becomes more anisotropic in component as the convective Mach number increases from $M_c = 0.2$ to 1.8, indicating the anisotropic suppression effect of compressibility on the mixing process.

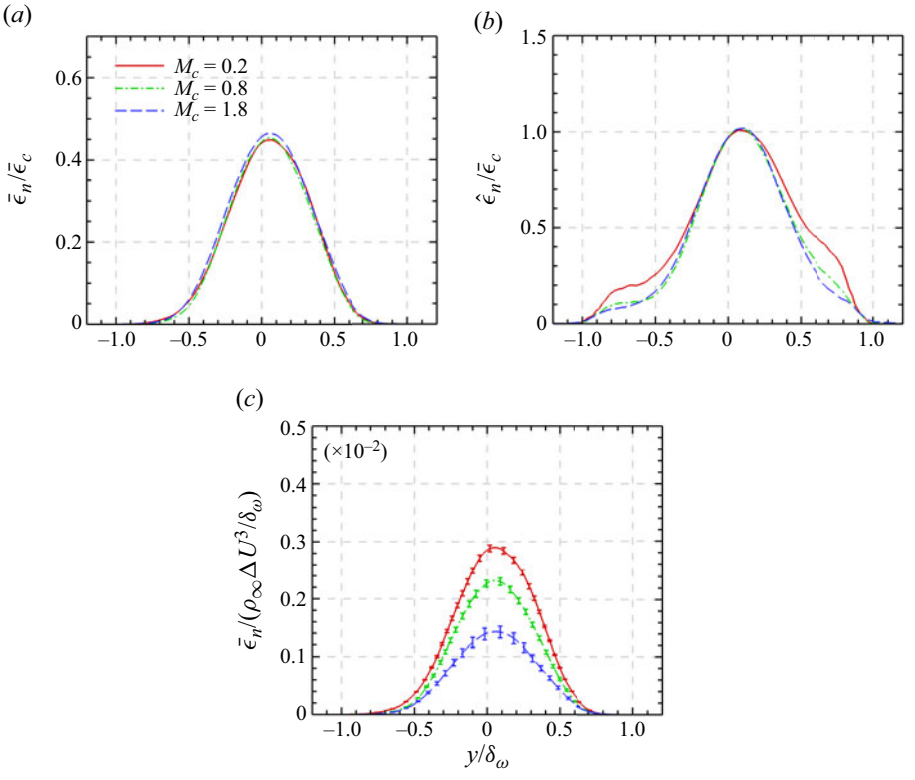

Figure 6. (*a*) Contributions of the low-speed LSSs to dissipation $\bar{\epsilon}_n/\bar{\epsilon}_c$ and (*b*) conditionally averaged dissipation $\hat{\epsilon}_n/\bar{\epsilon}_c$ based on low-speed events with $u'' < 0$ at $M_c = 0.2$, 0.8 and 1.8. (*c*) $\bar{\epsilon}_n$ is normalized by $\rho_\infty \Delta U^3/\delta_\omega$ with the error bar representing discrepancy among the maximum and minimum dissipation components.

Figure 7 shows two-dimensional conditionally averaged dissipation $\breve{\epsilon}_{i,n}/\bar{\epsilon}_c$ and streamwise velocity $\breve{u}_n/\Delta U$ based on the condition of $u'' < -0.15\Delta U$ at convective Mach numbers $M_c = 0.2$ and 1.8. The dissipation concentrates in the upper regions of the low-speed LSSs due to the modulation effect exerted by the LSSs on the small-scale structures, wherein the small-scale vortical structures are activated at the top of low-speed LSSs. This modulation effect was initially identified and extensively studied in wall turbulence (Marusic *et al.* 2010; Pirozzoli & Bernardini 2011; Chan & Chin 2022) and was observed in compressible mixing layers (Wang *et al.* 2022). At $M_c = 0.2$, the dissipation is concentrated in the upper part of the LSSs, exhibiting downstream skewness along the flow, with similar distributions and strengths across its components. At $M_c = 1.8$, dissipation within the LSSs exhibits noticeable component anisotropy. The dissipation in the flow direction predominates significantly over the other two components, while the spanwise component remains intermediate, and the vertical component is the smallest.

4.4. *Conversion between kinetic and internal energies*

Figure 8(*a*) shows the contribution of low-speed LSSs to the pressure-dilatation term $\bar{\Phi}_n/\bar{\epsilon}_c$ at convective Mach numbers $M_c = 0.2$, 0.8, 1.8. The pressure-dilatation term represents the energy exchange between turbulent kinetic energy and internal energy, and is significantly smaller than the dissipation term. At convective Mach number $M_c = 0.2$,

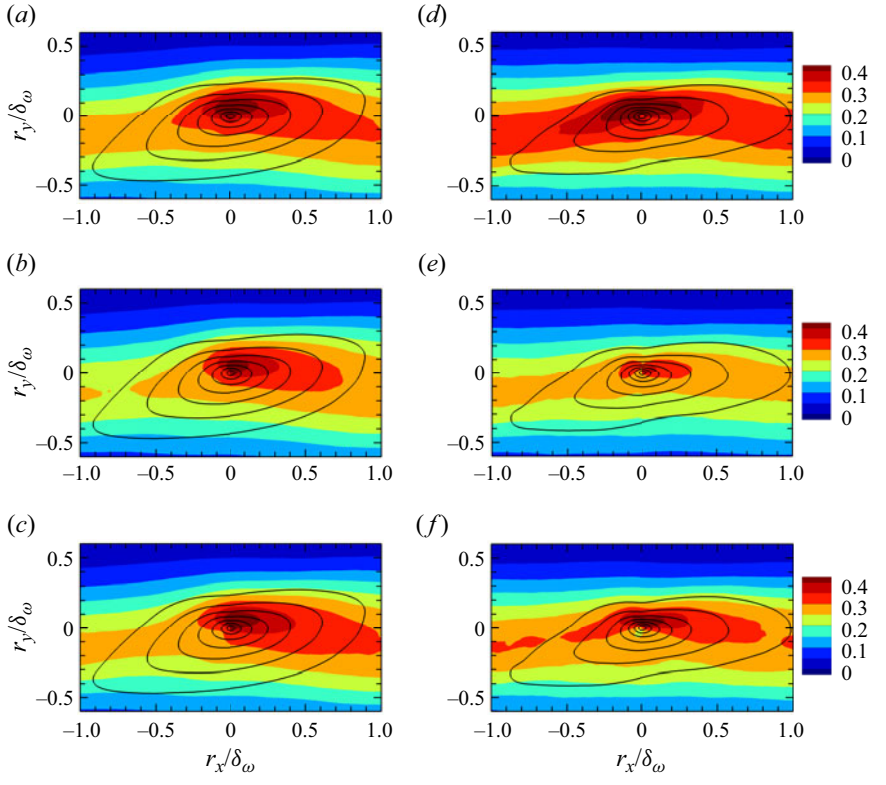

Figure 7. Two-dimensional conditionally averaged components of dissipation $\breve{\epsilon}_{i,n}/\bar{\epsilon}_c$ (contours) and streamwise velocity $\breve{u}_n/\Delta U$ (solid lines) based on low-speed events with $u'' < -0.15\Delta U$ at (*a–c*) $M_c = 0.2$ and (*d–f*) 1.8. (*a*,*d*) Streamwise, (*b*,*e*) vertical and (*c*,*f*) spanwise components.

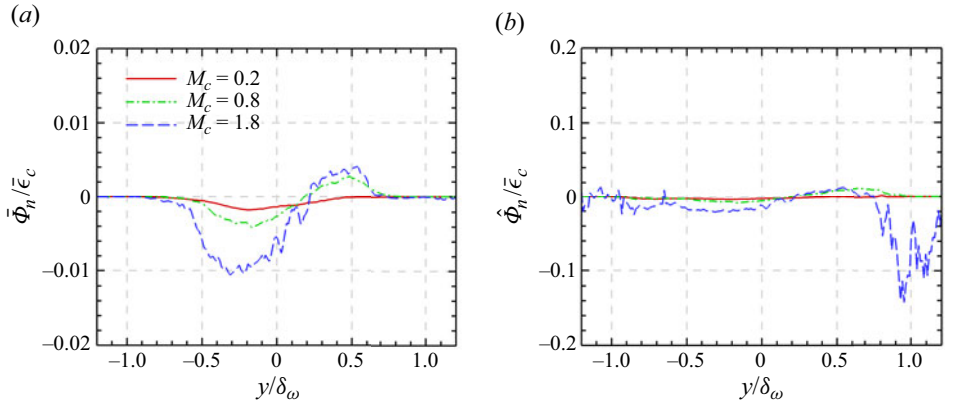

Figure 8. (*a*) Contributions of the low-speed LSSs to pressure-dilatation $\bar{\Phi}_n/\bar{\epsilon}_c$ and (*b*) conditionally averaged pressure-dilatation $\hat{\Phi}_n/\bar{\epsilon}_c$ based on low-speed events with $u'' < 0$ at $M_c = 0.2$, 0.8 and 1.8.

the pressure-dilatation term $\bar{\Phi}_n/\bar{\epsilon}_c$ is negative almost everywhere with its minimum at $y/\delta_\omega = -0.2$, indicating that the mean pressure-dilatation converts turbulent kinetic energy into internal energy within the LSSs. As the convective Mach number increases from $M_c = 0.2$ to 1.8, the magnitude of the minimum value of $\bar{\Phi}_n/\bar{\epsilon}_c$ increases, and the location of this minimum shifts slightly downwards. At higher convective Mach numbers

$M_c = 0.8$ and 1.8, $\bar{\Phi}_n/\bar{\epsilon}_c$ becomes positive for $y/\delta_\omega > 0.2$, peaking at $y/\delta_\omega = 0.5$. This observation implies that pressure-dilatation converts internal energy into the turbulent kinetic energy at the upper region of low-speed LSSs where the small-scale structures are concentrated. The contribution of low-speed LSSs to mean pressure-dilatation $\bar{\Phi}_n/\bar{\epsilon}_c$ increases with enhanced compressibility, but it still remains almost two orders of magnitude smaller than the production and dissipation terms, and has usually been neglected in previous literature (Pantano & Sarkar 2002; Arun *et al.* 2019).

However, the local pressure-dilatation can reach the same order of magnitude as the dissipation term near the edges of the mixing layer, as shown in figure 8(*b*), where the conditionally averaged pressure-dilatation term conditioned on the low-speed LSSs $\hat{\Phi}_n/\bar{\epsilon}_c$ obtains a minimum of -0.15 at $y/\delta_\omega = 0.9$ at the highest convective Mach number $M_c = 1.8$, even exceeding the magnitude of dissipation at the corresponding locations. It is clearly observed that at $M_c = 1.8$, the pressure-dilatation fluctuates significantly near the upper edge of the mixing layer. Additionally, beyond the upper edge of the mixing layer, at $y/\delta_\omega > 1.0$, there is still noticeable negative pressure-dilatation, whereas near the lower boundary of the mixing layer, the magnitude of pressure-dilatation is much smaller. This is likely related to the formation of shock waves. Rossmann, Mungal & Hanson (2002) and Zhou, He & Shen (2012) discovered that the shock formation mechanism closely resembles the scenario of high-speed flow around a bluff body. In other words, the upward-moving low-speed LSSs act like bulges of turbulent fluid protruding into the high-speed free stream, leading to the formation of shock waves propagating outwards from the surfaces of these LSSs. The formation of shock waves results in a dramatic conversion of turbulent kinetic energy into internal energy.

4.5. *Inter-component energy transfer*

The pressure-strain components are responsible for redistributing turbulent kinetic energy from the streamwise direction to the vertical and spanwise directions on average in turbulent mixing layers (Pantano & Sarkar 2002; Arun *et al.* 2019). Figures 9(*a*), 9(*c*) and 9(*e*) show the contribution of low-speed LSSs to the pressure-strain components $\bar{\Phi}_{i,n}/\bar{\epsilon}_c$ at convective Mach numbers $M_c = 0.2$, 0.8, 1.8. The three pressure-strain components $\bar{\Phi}_{i,n}/\bar{\epsilon}_c$ are of the same order of magnitude as the dominant budget terms including production and dissipation. The profiles of all pressure-strain components $\bar{\Phi}_{i,n}/\bar{\epsilon}_c$ exhibit a unimodal shape with their peaks located in the upper half of the mixing layer, demonstrating that the contribution of the low-speed LSSs to the component redistribution of turbulent kinetic energy concentrates in the upper half of the mixing layer. The redistribution predominantly occurs within the region $-0.5 < y/\delta_\omega < 0.7$, where the streamwise component $\bar{\Phi}_{1,n}/\bar{\epsilon}_c$ is negative, while both $\bar{\Phi}_{2,n}/\bar{\epsilon}_c$ and $\bar{\Phi}_{3,n}/\bar{\epsilon}_c$ components are positive, with their magnitudes being nearly identical to each other. This result indicates that the energy loss from the streamwise component is equally redistributed to the vertical and spanwise components.

Near the edge of the mixing layer, $\bar{\Phi}_{i,n}/\bar{\epsilon}_c$ is obviously non-zero for $y/\delta_\omega < -0.5$ and $y/\delta_\omega > 0.7$. Similar to the dissipation, the volume fraction corresponding to the pressure redistribution process near the mixing layer edge is small, but the magnitude of the pressure-strain components is not negligible. This is evident in the conditionally averaged pressure-strain components $\hat{\Phi}_{i,n}/\bar{\epsilon}_c$ shown in figures 9(*d*)–9(*f*). Within region $-1.0 < y/\delta_\omega < -0.5$, both $\hat{\Phi}_{1,n}/\bar{\epsilon}_c$ and $\hat{\Phi}_{3,n}/\bar{\epsilon}_c$ exhibit a negative peak, while $\hat{\Phi}_{2,n}/\bar{\epsilon}_c$ shows a positive peak, even reaching twice the magnitude of its peak observed in the

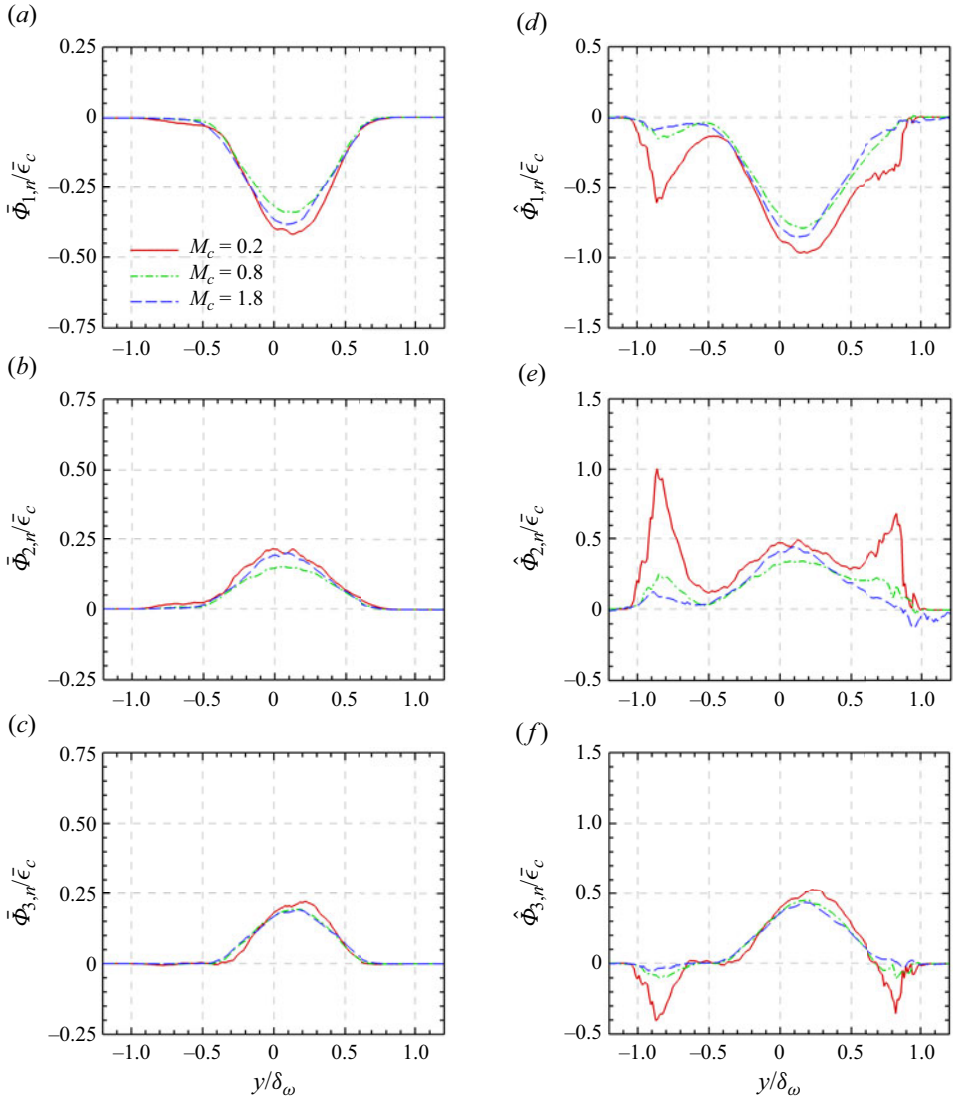

Figure 9. (*a–c*) Contributions of the low-speed LSSs to pressure-strain $\bar{\Phi}_{i,n}/\bar{\epsilon}_c$ and (*d–f*) conditionally averaged pressure-strain $\hat{\Phi}_{i,n}/\bar{\epsilon}_c$ based on low-speed events with $u'' < 0$ at $M_c = 0.2$, 0.8 and 1.8. (*a*,*d*) Streamwise, (*b*,*e*) vertical and (*c*,*f*) spanwise components.

central region of the mixing layer at low convective Mach number $M_c = 0.2$. These peaks are all located around $y/\delta_\omega \approx -0.85$. The observation indicates that both streamwise and spanwise turbulent kinetic energy are simultaneously converted to the vertical direction near the edge of the mixing layer. This can be attributed to the dynamics of the TNTI. A key characteristic of the TNTI is the well-known vorticity jump (or strong velocity gradient) across the interface, which resembles a shear layer that can become unstable under certain conditions. This unstable shear layer can cause the formation of secondary Kelvin–Helmholtz instabilities, which are linked to the nibbling process at the TNTI (Philip *et al.* 2014; Reuther & Kähler 2020). The secondary Kelvin–Helmholtz instabilities redistribute turbulent kinetic energy by converting the horizontal components into the

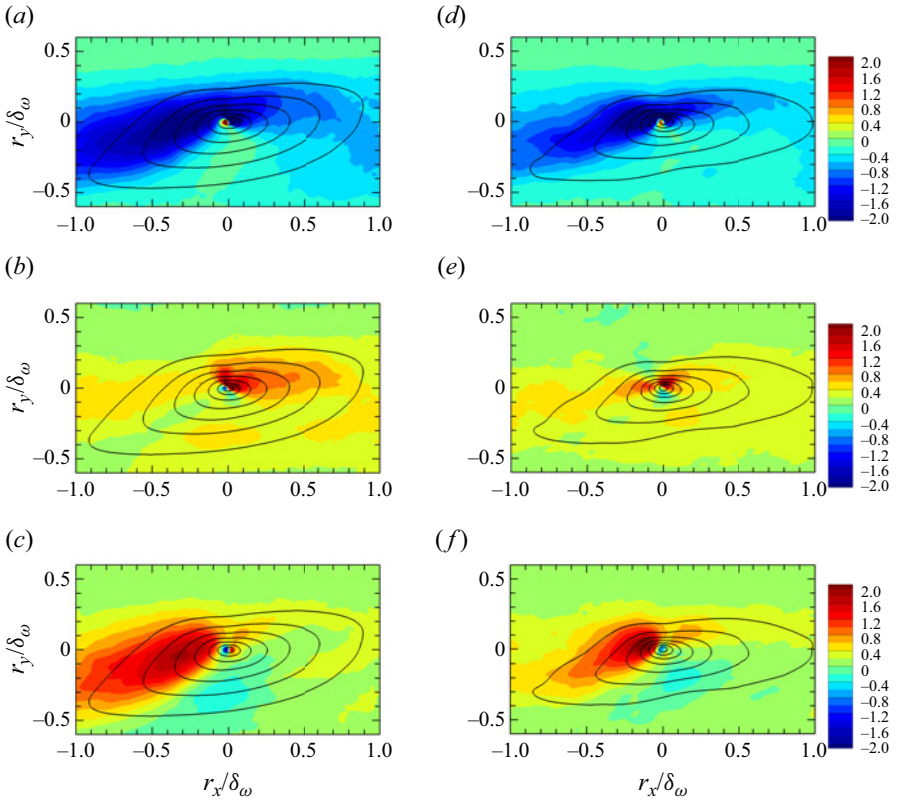

Figure 10. Two-dimensional conditionally averaged components of pressure-strain $\breve{\Phi}_{i,n}/\bar{\epsilon}_c$ (contours) and streamwise velocity $\breve{u}_n/\Delta U$ (solid lines) based on low-speed events with $u'' < -0.15\Delta U$ at (*a–c*) $M_c = 0.2$ and (*d–f*) 1.8. (*a*,*d*) Streamwise, (*b*,*e*) vertical and (*c*,*f*) spanwise components.

vertical component. Similarly, at the upper edge of the mixing layer, within the region $0.5 < y/\delta_\omega < 1.0$, the exchange of streamwise and spanwise turbulent kinetic energy to the normal direction also occurs, albeit with relatively weaker intensity. It is interesting to note that the peaks of the conditionally averaged pressure-strain $\hat{\Phi}_{i,n}/\bar{\epsilon}_c$ near the edges of the mixing layer rapidly decrease with the increase in convective Mach number, whereas the peaks in the central region of the mixing layer remain insensitive to the convective Mach number. This observation may be due to the fact that the pressure redistribution process occurs at both large and small scales. The large scales contribute more significantly to the overall redistribution, while the small scales exhibit more intense activity (Lee & Moser 2019; Wang *et al.* 2021). The increase in compressibility noticeably suppresses the pressure redistribution process associated with the small-scale structures. When normalized by $\rho_\infty \Delta U^3/\delta_\omega$, the pressure-strain terms exhibit a significant decrease with increasing Mach number, and are omitted here for the sake of brevity. In agreement with previous investigations, the decreasing of the pressure-strain term with increasing M_c leads to inhibited energy redistributing from the streamwise to cross-stream fluctuations, to the reduced turbulence production and, finally, to reduced turbulence levels as well as reduced growth rate of the shear layer (Vreman *et al.* 1996; Pantano & Sarkar 2002; Mahle 2007).

Figure 10 shows two-dimensional conditionally averaged pressure-strain $\breve{\Phi}_{i,n}/\bar{\epsilon}_c$ and velocity $\breve{u}_n/\Delta U$ based on the condition of $u'' < -0.15\Delta U$ at convective Mach numbers

$M_c = 0.2$ and 1.8. Although, on average, energy is evenly redistributed from streamwise to vertical and spanwise directions, the shapes of $\breve{\Phi}_{2,n}/\bar{\epsilon}_c$ and $\breve{\Phi}_{3,n}/\bar{\epsilon}_c$ in low-speed LSSs are completely different. This observation indicates a highly non-uniform redistribution of turbulent kinetic energy from the streamwise to the vertical and spanwise directions at the same location within LSSs. Far away from the centre of low-speed LSSs and biased towards the upstream direction, $\breve{\Phi}_{1,n}/\bar{\epsilon}_c$ and $\breve{\Phi}_{3,n}/\bar{\epsilon}_c$ display a large-scale region with strikingly similar shapes and large magnitude. In this region, $\breve{\Phi}_{1,n}/\bar{\epsilon}_c$ takes on a negative value, while $\breve{\Phi}_{3,n}/\bar{\epsilon}_c$ is positive. Thus, the streamwise turbulent kinetic energy K_1 is predominantly redistributed to the spanwise direction K_3. Near the centre of the LSSs and in a smaller region located above, there is a significant transfer of energy from K_1 to K_2, as shown in figures 10(*b*) and 10(*e*). Below the centre of the LSSs, at $(r_x/\delta_\omega, r_y/\delta_\omega) \approx (0.0, -0.2)$, $\breve{\Phi}_{3,n}/\bar{\epsilon}_c$ is negative, while $\breve{\Phi}_{1,n}/\bar{\epsilon}_c$ and $\breve{\Phi}_{2,n}/\bar{\epsilon}_c$ are positive, with relatively small magnitudes. Therefore, a small portion of turbulent kinetic energy is redistributed from K_3 to K_1 and K_2, primarily to K_2. The non-uniform redistribution shown in figures 9 and 10 is related to the pressure response caused by different scales. In the central region of the mixing layer, energy redistribution primarily occurs at larger scales, where the streamwise turbulent kinetic energy is transferred into the spanwise and vertical directions. Near the edges of the mixing layer, energy redistribution takes place at smaller scales, where turbulent kinetic energy shifts from the streamwise and spanwise components to the vertical component.

To further investigate the turbulent kinetic energy exchange among different components, we decompose the pressure-strain terms into positive and negative components: $\Phi_i = \Phi_i^+ + \Phi_i^-$, where the positive component $\Phi_i^+ = 0.5(\Phi_i + |\Phi_i|)$ and the negative component $\Phi_i^- = 0.5(\Phi_i - |\Phi_i|)$. The two-dimensional conditionally average of the positive and negative pressure-strain components are shown in figures 11 and 12 for $M_c = 0.2$ and 1.8, respectively. At low Mach number $M_c = 0.2$, the contours of $\breve{\Phi}_{i,n}^+/\bar{\epsilon}_c$ and $\breve{\Phi}_{i,n}^-/\bar{\epsilon}_c$ exhibit strikingly similar shapes, featuring a maximum value skewed towards the upper right side of the LSSs, with $\breve{\Phi}_{1,n}^+/\bar{\epsilon}_c$ having smaller magnitude. This observation indicates that each turbulent kinetic energy component not only receives energy from the other two directions, but also contributes energy to them simultaneously. At high Mach number $M_c = 1.8$, the magnitudes of $\breve{\Phi}_{i,n}^+/\bar{\epsilon}_c$ and $\breve{\Phi}_{i,n}^-/\bar{\epsilon}_c$ decrease and become more anisotropic compared with that at $M_c = 0.2$. Here, $\breve{\Phi}_{1,n}^-/\bar{\epsilon}_c$, $\breve{\Phi}_{2,n}^+/\bar{\epsilon}_c$ and $\breve{\Phi}_{3,n}^+/\bar{\epsilon}_c$ display two distinct peak regions in their contours, and are significantly larger than their respective counterparts. The transfer of energy from K_1 to K_2 predominantly occurs in a smaller-scale region at the upper right of the large-scale centre (at $r_x = 0$, $r_y = 0$), while the transfer from K_1 to K_3 takes place in a larger-scale region to the upper left of the large-scale centre. The exchange of turbulent kinetic energy between other components is notably reduced at $M_c = 1.8$.

4.6. *Spatial diffusion*

Figures 13(*a*)–13(*c*) show the contribution of low-speed LSSs to the turbulent diffusion of turbulent kinetic energy $\bar{T}_{t,i,n}/\bar{\epsilon}_c$ at convective Mach numbers $M_c = 0.2$, 0.8, 1.8. Turbulent diffusion exhibits a clear anisotropy. The streamwise component of turbulent diffusion is the largest, followed by the vertical component and the spanwise component is the smallest. The contribution of low-speed LSSs to the streamwise turbulent diffusion term, $\bar{T}_{t,1,n}/\bar{\epsilon}_c$, resembles a wave shape, with a phase shift upwards by approximately

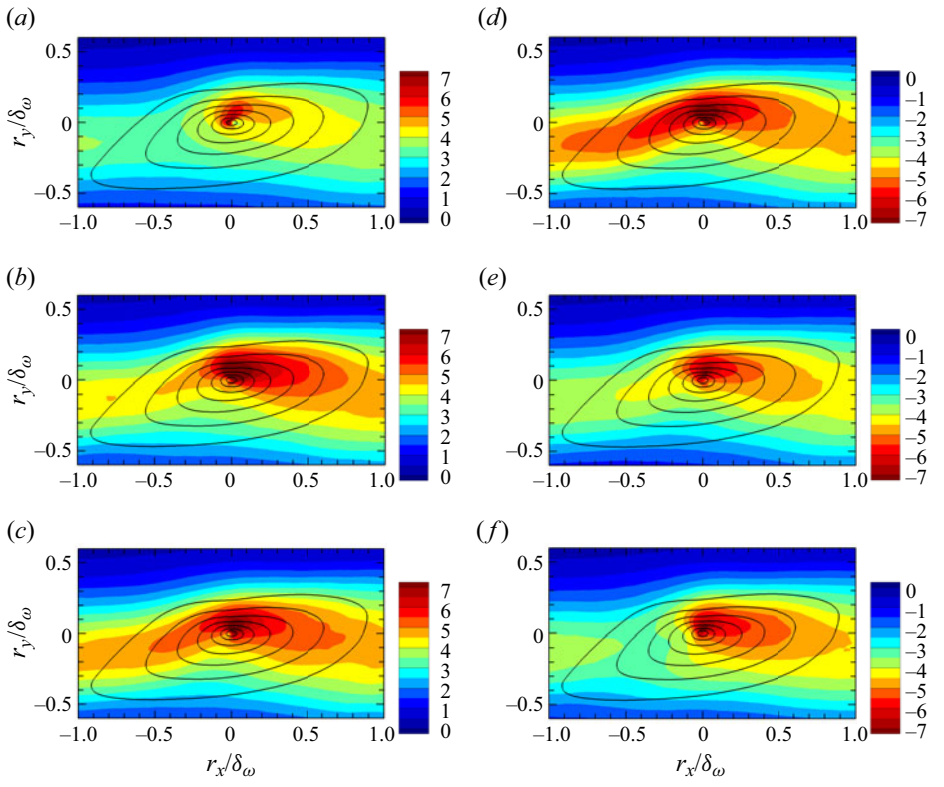

Figure 11. Two-dimensional conditionally averaged (*a–c*) positive part of pressure-strain $\breve{\Phi}^{+}_{i,n}/\bar{\epsilon}_c$, (*d–f*) negative part of pressure-strain $\breve{\Phi}^{-}_{i,n}/\bar{\epsilon}_c$ (contours) and streamwise velocity $\breve{u}_n/\Delta U$ (solid lines) based on low-speed events with $u'' < -0.15\Delta U$ at $M_c = 0.2$. (*a*,*d*) Streamwise, (*b*,*e*) vertical and (*c*,*f*) spanwise components.

$0.15/\delta_\omega$. The peak of this wave is located at $y/\delta_\omega = 0.4$, while the trough is positioned around $y/\delta_\omega = -0.15$. This observation indicates that within low-speed LSSs, $\bar{T}_{t,1,n}/\bar{\epsilon}_c$ transports streamwise turbulent kinetic energy K_1 upwards, whereas within high-speed LSSs, it transports K_1 downwards (not shown). It is interesting to note that the growth of $\bar{T}_{t,1,n}/\bar{\epsilon}_c$ from its trough to peak is nearly linear. Unlike the streamwise component, the vertical component of turbulent diffusion $\bar{T}_{t,2,n}/\bar{\epsilon}_c$ transports vertical turbulent kinetic energy K_2 from the centre of the mixing layer to both the upper and lower edges of the mixing layer simultaneously, although the downward transport is relatively minor. The spanwise component of turbulent diffusion $\bar{T}_{t,3,n}/\bar{\epsilon}_c$, however, behaves similarly to the vertical component, as it transports spanwise turbulent kinetic energy K_3 from the centre of the mixing layer to both the upper and lower edges of the mixing layer.

The conditionally averaged turbulent diffusion term $\hat{T}_{t,i,n}/\bar{\epsilon}_c$ is presented in figures 13(*d*)–13(*f*), where the local turbulent diffusion process is highlighted at the edges of the mixing layer. Here, $\hat{T}_{t,1,n}/\bar{\epsilon}_c$ peaks at $y/\delta_\omega = 0.7$, with an additional small trough appearing at $y/\delta_\omega = -0.7$. Additionally, $\hat{T}_{t,1,n}/\bar{\epsilon}_c$ exhibits linear growth from its minimum to maximum values. At $M_c = 0.2$ and 0.8, the range of this linear growth region expands to almost $y/\delta_\omega = 0.7$. Furthermore, the range of linear growth widens with decreasing convective Mach number, in contrast to the behaviour of the linear stage of volume

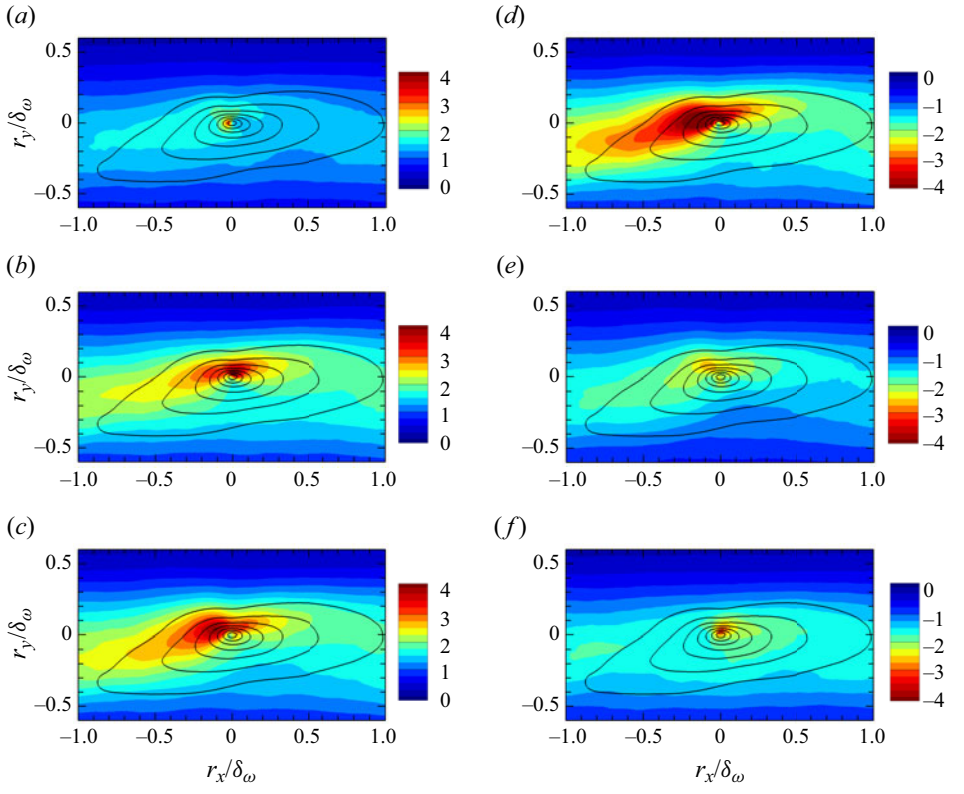

Figure 12. Two-dimensional conditionally averaged (*a–c*) positive part of pressure-strain $\breve{\Phi}^{+}_{i,n}/\bar{\epsilon}_c$, (*d–f*) negative part of pressure-strain $\breve{\Phi}^{-}_{i,n}/\bar{\epsilon}_c$ (contours) and streamwise velocity $\breve{u}_n/\Delta U$ (solid lines) based on low-speed events with $u'' < -0.15\Delta U$ at $M_c = 1.8$. (*a,d*) Streamwise, (*b,e*) vertical and (*c,f*) spanwise components.

fraction, as shown in figure 2(*a*). The two peaks of $\hat{T}_{t,2,n}/\bar{\epsilon}_c$ and $\hat{T}_{t,3,n}/\bar{\epsilon}_c$ have shifted to $y/\delta_\omega = \pm 0.8$. The vertical variation of $\hat{T}_{t,2,n}/\bar{\epsilon}_c$ is very large, especially at the edges of the mixing layer, where its peak near the upper edge even exceeds the peak of $\hat{T}_{t,1,n}/\bar{\epsilon}_c$. The magnitude of $\hat{T}_{t,3,n}/\bar{\epsilon}_c$ is noticeably smaller than the other two components. As the convective Mach number increases, the conditionally averaged turbulent diffusion term $\hat{T}_{t,i,n}/\bar{\epsilon}_c$ decreases rapidly near the edges of the mixing layer, while it remains relatively unchanged at the centre of the mixing layer.

More insight into the spatial distribution of the turbulent diffusion can be gained from its two-dimensional conditional average shown in figure 14. The streamwise turbulent diffusion features two large-scale regions of similar shapes, with positive values in the upper left and negative values in the lower right. This suggests that the streamwise turbulent diffusion $\breve{T}_{t,1,n}/\bar{\epsilon}_c$ transports streamwise turbulent kinetic energy from the lower right region of the low-speed LSSs to its upper left region. In other words, the direction of turbulent diffusion of K_1 is not vertical but inclined, with a skew angle of approximately 18° at $M_c = 0.2$ and 15° at 1.8. This angle is measured between the line (black dashed line figure 14*a,d*) connecting the extrema (maximum and minimum points) of the two large-scale regions and the horizontal direction. The direction of turbulent diffusion K_2 also tends to be from the lower right region of the LSSs towards its upper left region,

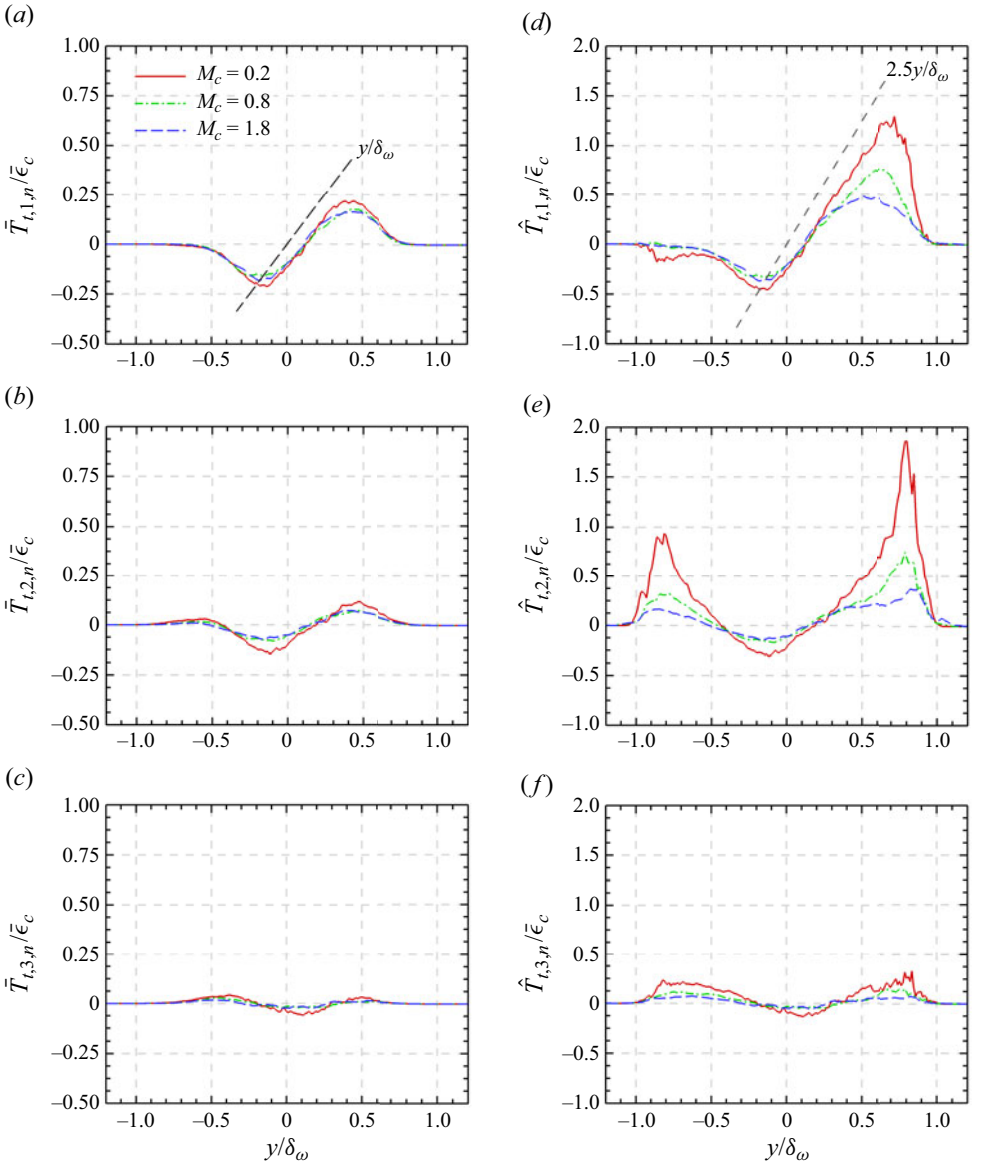

Figure 13. (*a–c*) Contributions of the low-speed LSSs to turbulent diffusion $\bar{T}_{t,i,n}/\bar{\epsilon}_c$ and (*d–f*) conditionally averaged turbulent diffusion $\hat{T}_{t,i,n}/\bar{\epsilon}_c$ based on low-speed events with $u'' < 0$ at $M_c = 0.2$, 0.8 and 1.8. (*a*,*d*) Streamwise, (*b*,*e*) vertical and (*c*,*f*) spanwise components.

but with a weaker intensity. However, the direction of turbulent diffusion K_3 tends to be from the upper left region of the LSSs towards its lower right region, opposite to the direction of K_1 and K_2. The inclined distribution of the turbulent diffusion components in the x–y plane causes positive and negative values to cancel each other out when averaged in the horizontal plane. As a result, the maximum positive and negative values of the turbulent diffusion components in the two-dimensional average shown in figure 14 are significantly larger than their counterparts in figures 13(*d*)–13(*f*), especially for the streamwise component of turbulent diffusion.

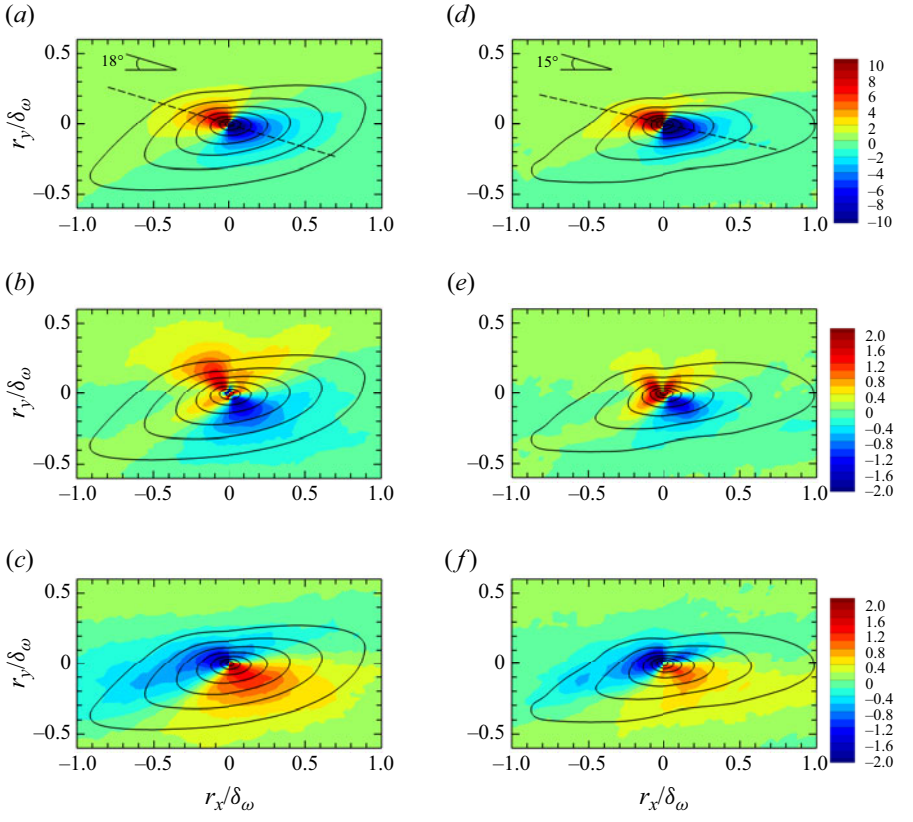

Figure 14. Two-dimensional conditionally averaged components of turbulent diffusion $\breve{T}_{t,i,n}/\bar{\epsilon}_c$ (contours) and streamwise velocity $\breve{u}_n/\Delta U$ (solid lines) based on low-speed events with $u'' < -0.15\Delta U$ at (*a–c*) $M_c = 0.2$ and (*d–f*) 1.8. (*a*,*d*) Streamwise, (*b*,*e*) vertical and (*c*,*f*) spanwise components.

Figures 15(*a*)–15(*c*) show the contribution of low-speed LSSs to the pressure diffusion of turbulent kinetic energy $\bar{T}_{p,i,n}/\bar{\epsilon}_c$ at convective Mach numbers $M_c = 0.2$, 0.8, 1.8. Compared with the turbulent diffusion, the value of pressure diffusion is much smaller. The magnitudes of the three components of pressure diffusion $\bar{T}_{p,i,n}/\bar{\epsilon}_c$ are comparable. The contribution of low-speed LSSs to the streamwise component of pressure diffusion $\bar{T}_{p,1,n}/\bar{\epsilon}_c$ also exhibits a wave shape, with its peak at $y/\delta_\omega = -0.5$ and its trough at $y/\delta_\omega = 0.2$. Thus, it transports streamwise turbulent kinetic energy K_1 from the upper to the lower part of the mixing layer, in contrast to the role of $\bar{T}_{t,1,n}/\bar{\epsilon}_c$. The vertical pressure diffusion term $\bar{T}_{p,2,n}/\bar{\epsilon}_c$ exhibits a positive peak located at $y/\delta_\omega \approx 0$, flanked by negative peaks on either side, with the upper negative peak stronger than the lower one, indicating that $\bar{T}_{p,2,n}/\bar{\epsilon}_c$ transports vertical turbulent kinetic energy K_2 from the edges of the mixing layer towards its centre, in contrast to the role of $\bar{T}_{t,2,n}/\bar{\epsilon}_c$. The distribution of $\bar{T}_{p,3,n}/\bar{\epsilon}_c$ along the y-direction is relatively complex, with its sign changing multiple times. In the range of $-0.7 < y/\delta_\omega < 0.5$, $\bar{T}_{p,3,n}/\bar{\epsilon}_c$ primarily transports K_3 from the upper to lower part of the mixing layer.

The conditionally averaged pressure diffusion term $\hat{T}_{p,i,n}/\bar{\epsilon}_c$ is presented in figures 15(*d*)–15(*f*), where the local pressure diffusion process is highlighted at the edges of the mixing layer. Here, $\hat{T}_{p,1,n}/\bar{\epsilon}_c$ peaks at $y/\delta_\omega = -0.8$. Additionally, $\hat{T}_{p,2,n}/\bar{\epsilon}_c$ is nearly

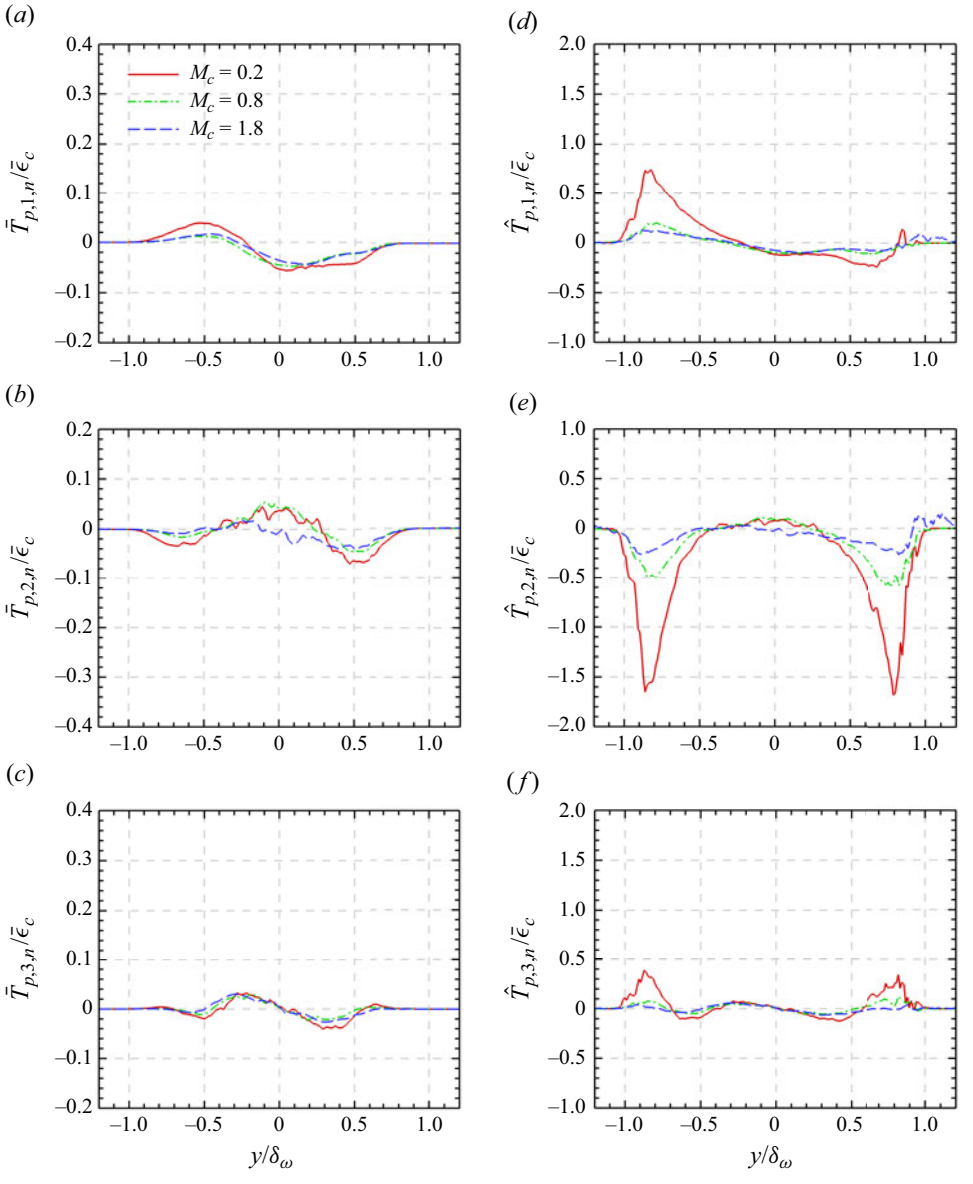

Figure 15. (*a–c*) Contributions of the low-speed LSSs to pressure diffusion $\bar{T}_{p,i,n}/\bar{\epsilon}_c$ and (*d–f*) conditionally averaged pressure diffusion $\hat{T}_{p,i,n}/\bar{\epsilon}_c$ based on low-speed events with $u'' < 0$ at $M_c = 0.2$, 0.8 and 1.8. (*a*,*d*) Streamwise, (*b*,*e*) vertical and (*c*,*f*) spanwise components.

symmetric about $y/\delta_\omega = 0$, exhibiting two remarkable negative peaks at $y/\delta_\omega = \pm 0.8$, with their magnitudes nearly equivalent to the maximum peak of $\hat{T}_{t,2,n}/\bar{\epsilon}_c$ (shown in figure 13*e*). At the edges of the mixing layer, $\hat{T}_{p,3,n}/\bar{\epsilon}_c$ exhibits two positive peaks, which are slightly larger than the two peaks of $\hat{T}_{t,3,n}/\bar{\epsilon}_c$ (shown in figure 13*f*) at the edges. As the convective Mach number increases, the conditionally averaged pressure diffusion term $\hat{T}_{p,i,n}/\bar{\epsilon}_c$ decreases rapidly near the edges of the mixing layer.

Figure 16 presents the two-dimensional conditional average of the pressure diffusion $\breve{T}_{p,i,n}/\bar{\epsilon}_c$ at $M_c = 0.2$ and 1.8. On the left side of the centre of low-speed LSSs, there exists

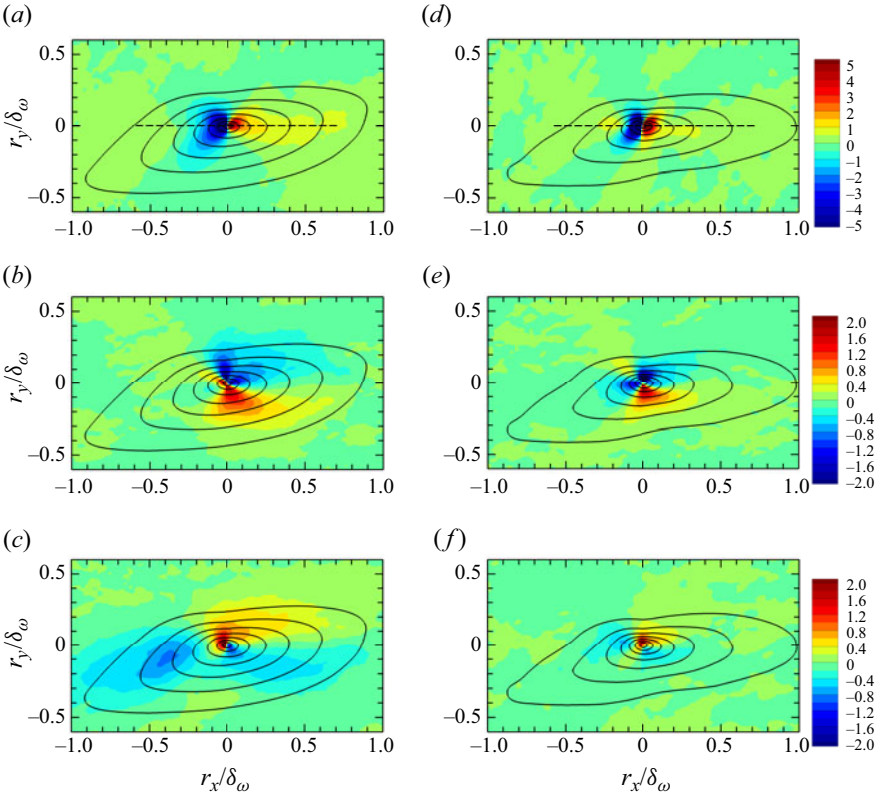

Figure 16. Two-dimensional conditionally averaged components of pressure diffusion $\breve{T}_{p,i,n}/\bar{\epsilon}_c$ (contours) and streamwise velocity $\breve{u}_n/\Delta U$ (solid lines) based on low-speed events with $u'' < -0.15\Delta U$ at (*a–c*) $M_c = 0.2$ and (*d–f*) 1.8. (*a*,*d*) Streamwise, (*b*,*e*) vertical and (*c*,*f*) spanwise components.

a large-scale region where the streamwise component of pressure diffusion is negative, while on the right side, there is a large-scale region with positive streamwise pressure diffusion. The black dashed line connecting the extrema (maximum and minimum points) of the two large-scale regions is almost horizontal, as shown in figures 16(*a*) and 16(*d*). This suggests that within low-speed LSSs, the streamwise pressure diffusion component $\breve{T}_{p,1,n}/\bar{\epsilon}_c$ primarily transports K_1 from left to right, and its non-uniformity nearly leads to the transport of K_1 from top to bottom, as shown in figure 15(*a*). The distribution of streamwise pressure diffusion components in the x–y plane leads to a more pronounced effect of positive and negative values cancelling each other out when averaged in the horizontal plane. The two-dimensional distributions of the vertical and spanwise components of pressure diffusion are relatively complex, but the overall trend is to transport the vertical and spanwise turbulent kinetic energy downwards. At higher convective Mach number $M_c = 1.8$, the pressure diffusion occurs within a smaller region.

The three components of viscous diffusion $\bar{T}_{v,i,n}$ are each an order of magnitude smaller than turbulent diffusion and pressure diffusion across all three convective Mach numbers; therefore, they are not further analysed here for brevity.

4.7. *Mass flux coupling*

According to the definition of the mass flux coupling term (3.3*f*), its ensemble average is very small because the Favre average of u'' is zero (Pantano & Sarkar 2002).

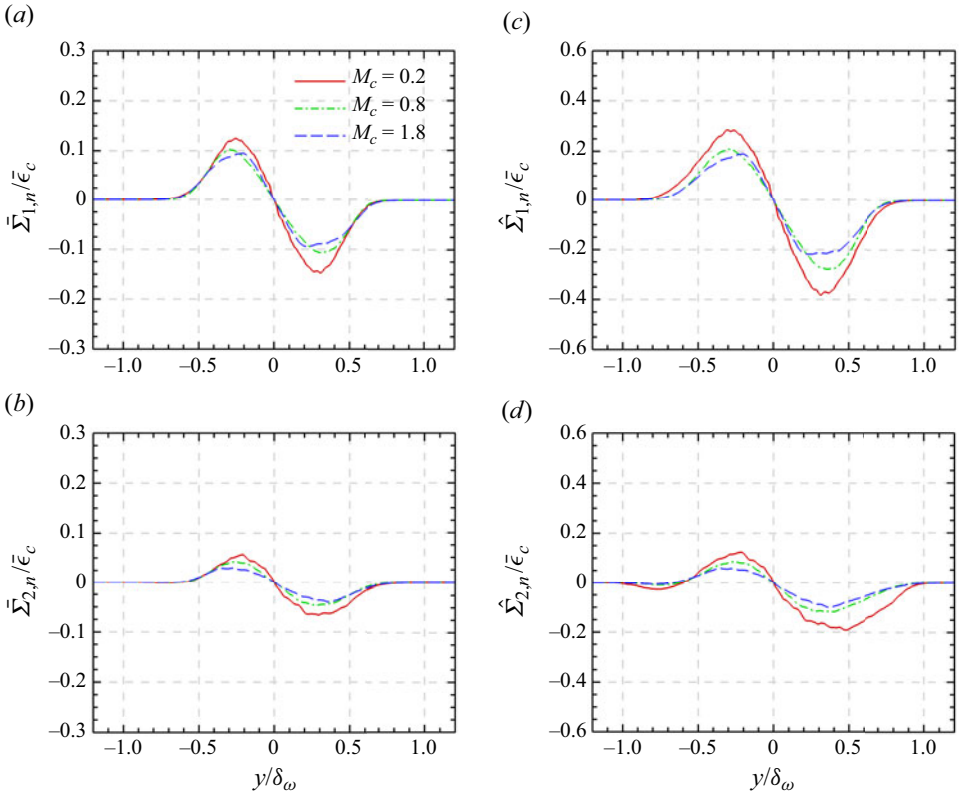

Figure 17. (*a*,*b*) Contributions of the low-speed LSSs to mass flux coupling $\bar{\Sigma}_{i,n}/\bar{\epsilon}_c$ and (*c*,*d*) conditionally averaged mass flux coupling $\hat{\Sigma}_{i,n}/\bar{\epsilon}_c$ based on low-speed events with $u'' < 0$ at $M_c = 0.2$, 0.8 and 1.8. (*a*,*c*) Streamwise and (*b*,*d*) vertical components.

The conditional averages of u'' and v'' are of the order of ΔU, as shown in figures 5(*a*) and 5(*b*), while the conditional average of w'' remains negligible. Consequently, the conditional average of the mass flux coupling term within LSSs is not zero. Figures 17(*a*) and (17*b*) show the contribution of low-speed LSSs to the mass flux coupling term $\bar{\Sigma}_{i,n}/\bar{\epsilon}_c$ at convective Mach numbers $M_c = 0.2, 0.8, 1.8$. The contribution of low-speed LSSs to the streamwise mass flux coupling term $\bar{\Sigma}_{1,n}/\bar{\epsilon}_c$ exhibits a positive peak at $y/\delta_\omega = -0.25$ and it displays a negative trough at $y/\delta_\omega = 0.25$, with the magnitudes of its peak and trough being almost equal. Considering the symmetry of high- and low-speed LSSs, $\bar{\Sigma}_{1,p}/\bar{\epsilon}_c$ and $\bar{\Sigma}_{1,n}/\bar{\epsilon}_c$ are symmetrical about the origin point, which means that they nearly cancel each other out, resulting in $\bar{\Sigma}_1$ being nearly zero. The characteristics of $\bar{\Sigma}_{2,n}/\bar{\epsilon}_c$ are very similar to those of $\bar{\Sigma}_{1,n}/\bar{\epsilon}_c$, except the magnitudes of the peaks and troughs are somewhat smaller. These results indicate that $\bar{\Sigma}_{1,n}/\bar{\epsilon}_c$ and $\bar{\Sigma}_{2,n}/\bar{\epsilon}_c$ transport streamwise and vertical turbulent kinetic energy downwards, respectively.

The conditionally averaged mass flux coupling term $\hat{\Sigma}_{i,n}/\bar{\epsilon}_c$ is presented in figures 17(*c*) and 17(*d*). The trough values of $\hat{\Sigma}_{i,n}/\bar{\epsilon}_c$ are slightly larger than the peak values. At the edges of the mixing layer, the local values of the mass flux coupling term do not exhibit significant amplification, unlike the other budget terms. Here, $\hat{\Sigma}_{2,n}/\bar{\epsilon}_c$ shows a minor trough near the lower edge, indicating a small amount of vertical turbulent

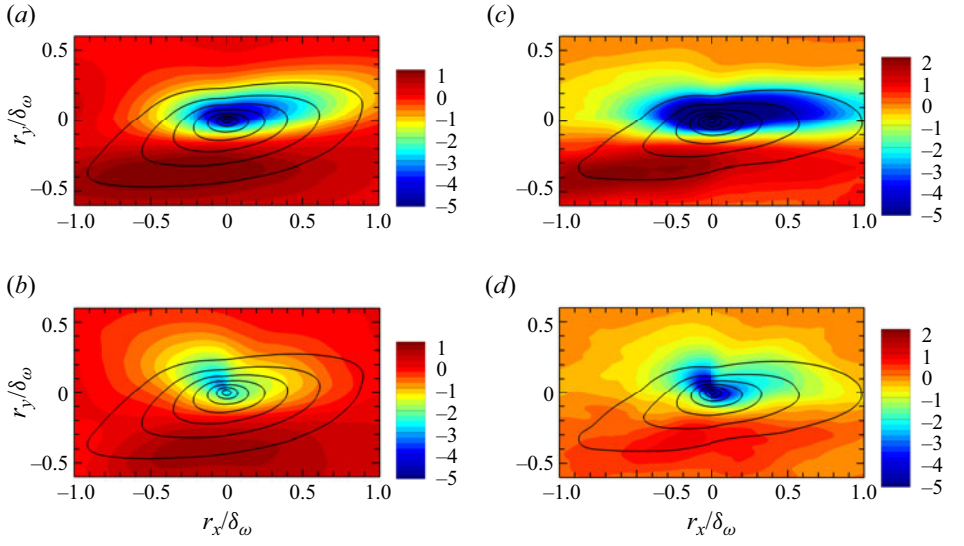

Figure 18. Two-dimensional conditionally averaged mass flux coupling $\breve{\Sigma}_{i,n}/\bar{\epsilon}_c$ (contours) and streamwise velocity $\breve{u}_n/\Delta U$ (solid lines) based on low-speed events with $u'' < -0.15\Delta U$ at (*a*,*b*) $M_c = 0.2$ and (*c*,*d*) 1.8. (*a*,*c*) Streamwise and (*b*,*d*) vertical components.

kinetic energy is transported upwards into the turbulent region. The spanwise mass flux coupling term is negligible and is omitted here for the sake of brevity. Figure 18 shows two-dimensional conditionally averaged mass flux coupling $\breve{\Sigma}_{i,n}/\bar{\epsilon}_c$ based on the condition of $u'' < -0.15\Delta U$ at convective Mach numbers $M_c = 0.2$ and 1.8. Both the streamwise and vertical components of mass flux coupling exhibit a relatively strong negative region in the upper part of the LSSs and a weaker positive region in the lower part, qualitatively consistent with figures 17(*c*) and 17(*d*).

4.8. *Total variation of turbulent kinetic energy in LSSs*

Figures 19(*a*)–19(*c*) show the contribution of low-speed LSSs to the total variation of turbulent kinetic energy, $\bar{V}_{i,n}/\bar{\epsilon}_c$, at convective Mach numbers $M_c = 0.2$, 0.8, 1.8. The contribution of low-speed LSSs to the total variation of streamwise turbulent kinetic energy $\bar{V}_{1,n}/\bar{\epsilon}_c$ exhibits two distinct positive peaks: a larger one in the upper half and a smaller one in the lower half of the mixing layer. Additionally, $\bar{V}_{2,n}/\bar{\epsilon}_c$ exhibits a distinct double-peak distribution, while $\bar{V}_{3,n}/\bar{\epsilon}_c$ shows a positive peak only in the upper half of the mixing layer and is nearly zero in the lower half. Near the centre of the mixing layer, $\bar{V}_{2,n}/\bar{\epsilon}_c$ and $\bar{V}_{3,n}/\bar{\epsilon}_c$ are almost zero, whereas $\bar{V}_{1,n}/\bar{\epsilon}_c$ shows a small negative value, indicating a reduction in streamwise turbulent kinetic energy K_1 at this position. This suggests that even at the centre, the mixing layer has not achieved a completely self-similar state. As the convective Mach number increases, $\bar{V}_{i,n}/\bar{\epsilon}_c$ decreases and the peak of $\bar{V}_{2,n}/\bar{\epsilon}_c$ in the lower half almost disappears at $M_c = 1.8$.

The conditionally averaged total variation $\hat{V}_{i,n}/\bar{\epsilon}_c$ is presented in figures 15(*d*)–15(*f*). Near the upper edge of the mixing layer, the total variation of K_1 is very prominent, with a peak at $y/\delta_\omega \approx 0.7$. In contrast, near the lower edge, the total variation of K_1 is nearly zero and surprisingly negative at $M_c = 0.2$. The total variations of K_2 and K_3 both exhibit significant positive peaks near both edges of the mixing layer, with the peak at

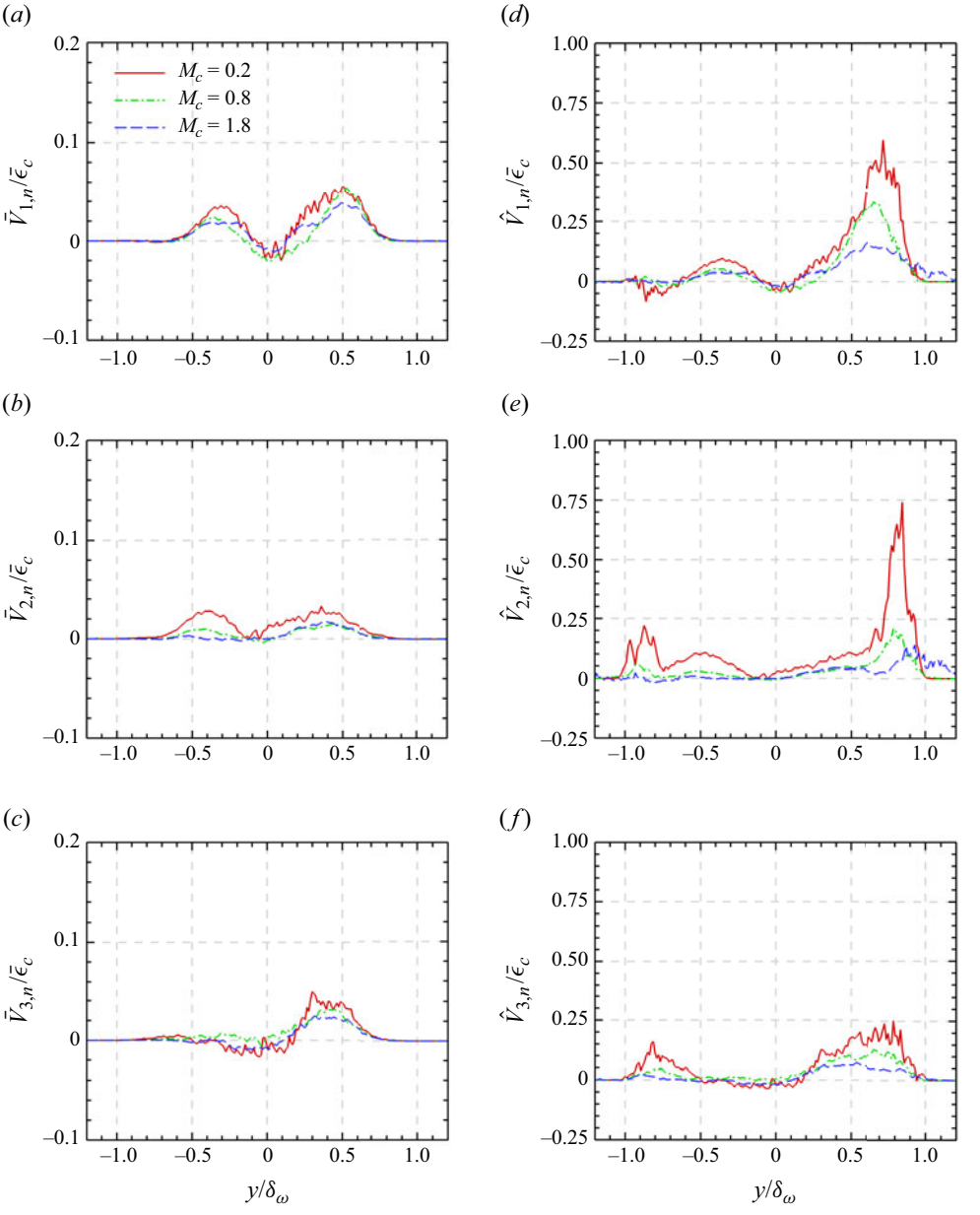

Figure 19. (*a–c*) Contributions of the low-speed LSSs to the total variation of turbulent kinetic energy $\bar{V}_{i,n}/\bar{\epsilon}_c$ and (*d–f*) conditionally averaged total variation $\hat{V}_{i,n}/\bar{\epsilon}_c$ based on low-speed events with $u'' < 0$ at $M_c = 0.2$, 0.8 and 1.8. (*a*,*d*) Streamwise, (*b*,*e*) vertical and (*c*,*f*) spanwise components.

the upper edge being larger. The total variation of K_2 near the upper edge, at $y/\delta_\omega \approx 0.7$, is particularly notable, even exceeding the value of K_1. As the convective Mach number increases, the total variations of turbulent kinetic energy in all three directions decrease significantly at the edges. These results further confirm the amplitude modulation effect of LSSs on small-scale structures at the edges of the mixing layer, consistent with the findings shown in figures 3(*d*)–3(*f*). The level of amplitude modulation is strongest for the vertical

velocity, followed by the streamwise velocity and weakest for the spanwise velocity. Additionally, the amplitude modulation decreases significantly with increasing Mach number. The entrainment process is usually associated with two mechanisms: nibbling, which is considered to be carried out by small-scale structures and plays the main role, and engulfment, which is mostly due to large-scale eddies (Westerweel *et al.* 2005; da Silva *et al.* 2014; Jahanbakhshi & Madnia 2016). We infer that with increasing convective Mach number, the level of amplitude modulation decreases significantly, resulting in weakened small-scale structures near the edge of the mixing layer. This leads to an evident increase in the normalized Kolmogorov length scale η/δ_ω, indicating a reduction in scale separation, as reported by Wang *et al.* (2024). Krug *et al.* (2015) proposed a relationship estimating the surface area A of the TNTI, where $A \propto (\eta/\delta_\omega)^{-1/3}$. Based on this relationship, we can infer that the TNTI surface area decreases as the small-scale structures weaken. The reduction in TNTI surface area, in turn, decreases the mass flow rate associated with nibbling, as reported by Jahanbakhshi & Madnia (2016).

5. Conclusion

DNS of compressible temporally developing mixing layers have been performed to investigate the impact of LSSs on the turbulent kinetic energy budgets in physical space and to further clarify the growth suppression mechanism associated with compressibility effects. Three cases with convective Mach number, M_c, from 0.2 to 1.8 are analysed. In the present study, high- and low-speed LSSs are identified as negative and positive regions of fluctuating streamwise velocity u''. In the core region of mixing layers, the volume fraction of low-speed LSSs decreases linearly with a coefficient of 0.165 that is independent on the convective Mach number. As the convective Mach number increases, the linear region of the volume fraction extends over a broader range.

The contributions of LSSs to the turbulent kinetic energy and their budgets are evaluated by decomposing them into three parts, representing the contributions from the low-speed LSSs, high-speed LSSs and engulfed regions in the mixing layer. The contributions of low-speed LSSs on turbulent kinetic energy, production, dissipation and pressure-strain are primarily concentrated in the region slightly above the centre of the mixing layer, while those of high-speed LSSs are concentrated slightly below the centre. The spatial diffusion and mass flux coupling terms are responsible for the vertical transport of turbulent kinetic energy. In low-speed LSSs, the streamwise component of turbulent diffusion transports K_1 upwards from the lower half to the upper half of the mixing layer, while the vertical and spanwise components of turbulent diffusion transport K_2 and K_3 from the middle to the edges of the mixing layer, respectively. In the core region of low-speed LSSs, the growth of streamwise turbulent diffusion is nearly linear. The pressure diffusion term acts with less intensity. The streamwise pressure diffusion transports K_1 downwards from the upper half to the lower half of the mixing layer, while the vertical and spanwise components of pressure diffusion transport K_2 and K_3 from the edges to the middle of the mixing layer, respectively. The streamwise and vertical mass flux coupling terms are comparable to the other dominant terms, and transport K_1 and K_2 downwards, respectively. The viscous diffusion and spanwise mass flux coupling terms are negligible in low-speed LSSs.

The spatial distribution of energy budget terms in low-speed LSSs is investigated through conditional averaging. The energy budgets near the edges of the mixing layer are dominated by small-scale structures. At the edges of LSSs, the sources and losses of all three components of turbulent kinetic energy are completely different to each other, and dominated by turbulent diffusion, pressure diffusion, pressure-strain and dissipation terms.

In low-speed LSSs, the streamwise turbulent kinetic energy near the upper edge originates from turbulent diffusion, while near the lower edge, it comes from pressure diffusion. Most of the streamwise turbulent kinetic energy is transferred to the vertical direction through pressure-strain, and the remaining small portion is dissipated by viscous effects. The vertical turbulent kinetic energy near both edges mainly originates from turbulent diffusion, with an additional portion coming from the streamwise and spanwise directions via pressure-strain. The loss of vertical turbulent kinetic energy is primarily due to pressure diffusion, which transports it to the interior of the LSSs, with a small portion dissipated by viscous effects. The spanwise turbulent kinetic energy comes from both turbulent diffusion and pressure diffusion. Most of it is transferred to the vertical direction through pressure-strain, while a small portion is dissipated by viscous effects.

The pressure-dilatation increases rapidly with the convective Mach number, but it is still an order of magnitude smaller than other terms. In the lower part of the low-speed LSSs, pressure-dilatation is negative, indicating that turbulent kinetic energy is converted to internal energy. In the upper part, pressure-dilatation is positive, converting internal energy to turbulent kinetic energy. At $M_c = 1.8$, strong negative pressure-dilatation appears at the upper edge of the low-speed LSSs due to the formation of noticeable shock waves, which rapidly converts turbulent kinetic energy to internal energy.

Finally, the analysis of the turbulent kinetic energy budget reveals the interaction between large-scale and small-scale structures in compressible turbulent mixing layers. The turbulent kinetic energy, their total variation and dissipation are significantly amplified at two edges of the mixing layer, which supports the existence of amplitude modulation exerted by the LSSs onto the near-edge small-scale structures. The level of amplitude modulation is strongest for the vertical velocity, followed by the streamwise velocity and weakest for the spanwise velocity. Additionally, the amplitude modulation decreases significantly with increasing Mach number in compressible mixing layers. The above results are meaningful for turbulence modelling, as they suggest the potential for developing predictive models for various budget terms of turbulent kinetic energy based on the amplitude modulation effect, similar to velocity prediction model proposed by Marusic *et al.* (2010).

Funding. This work was supported by the National Natural Science Foundation of China (NSFC grants 12172161, 92052301, 12161141017 and 91952104), by the NSFC Basic Science Center Program (grant no. 11988102), by the Shenzhen Science and Technology Program (grant no. KQTD20180411143441009) and by Department of Science and Technology of Guangdong Province (grant nos 2019B21203001, 2020B1212030001, 2023B1212060001). This work was also supported by Center for Computational Science and Engineering of Southern University of Science and Technology.

Declaration of interests. The authors report no conflict of interest.

Author ORCIDs.
Xiaoning Wang https://orcid.org/0000-0002-2616-6661;
Jianchun Wang https://orcid.org/0000-0001-5101-7791.

Appendix. Confinement effect of the computational domain

In this section, the confinement effect of the computational domain is investigated to validate the data. To minimize the effects of the finite domain size on the results, the two-point correlation should be small for large r. Figures 20 and 21 show that this condition is satisfied for the case with $M_c = 0.2$ and $M_c = 1.8$, respectively.

At $M_c = 1.8$, $\mathcal{R}_{xu}$ in the later part of the self-similar stage from $\tau = 2000$ to $\tau = 2250$ does not exhibit complete decay to zero decorrelation and $\mathcal{R}_{zu}$ does not return to zero

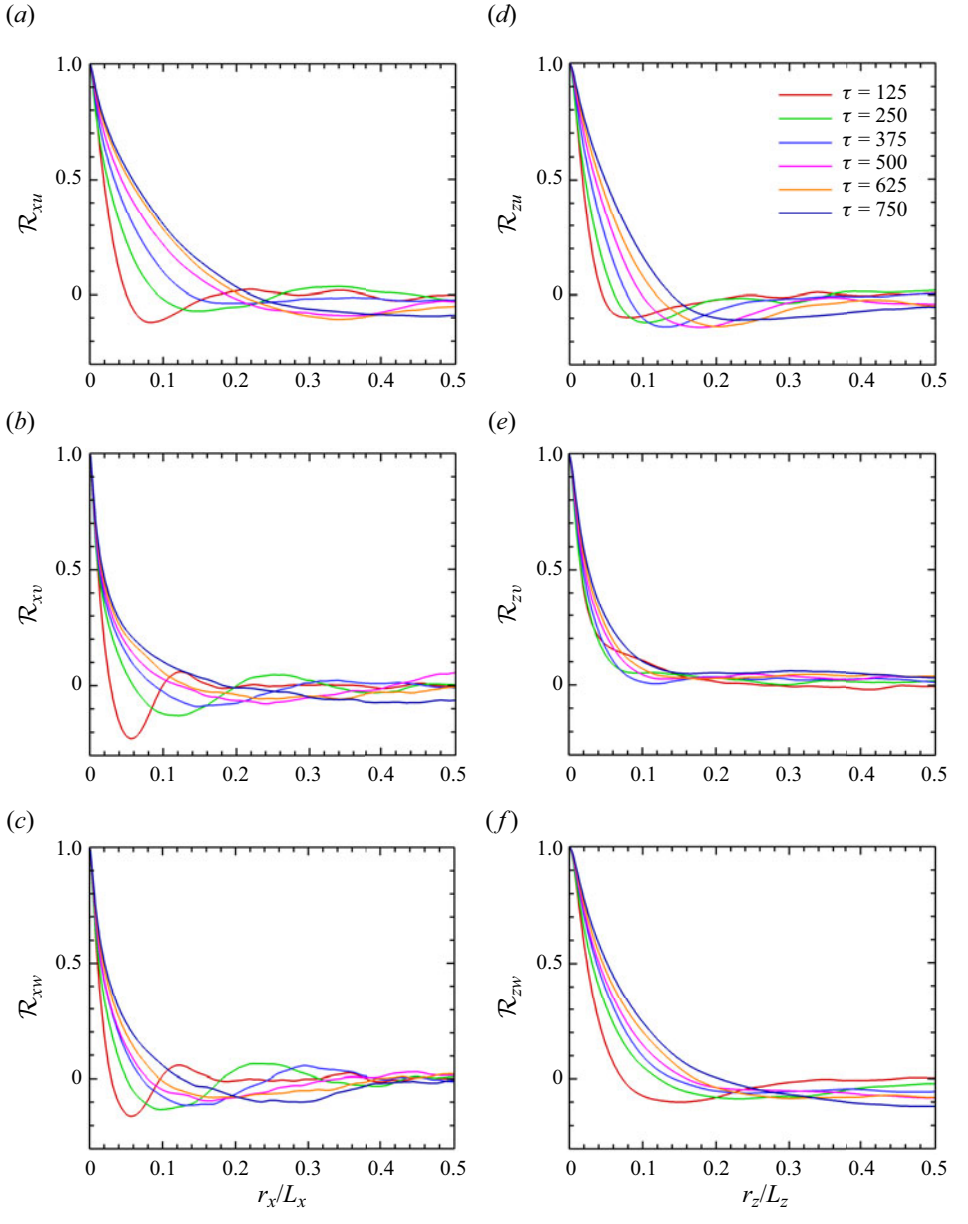

Figure 20. (*a–c*) Streamwise and (*d–f*) spanwise two-point correlations of (*a*,*d*) streamwise, (*b*,*e*) vertical and (*c*,*f*) spanwise velocities at the centreline at several time instants from $\tau = 125$ to $\tau = 750$ for the case with $M_c = 0.2$.

after the negative correlation, as shown in figures 21(*a*) and 21(*d*), since the scale of the high- and low-speed LSSs have become comparable to the size of the computational domain. Similar behaviour has been observed in the results of Vaghefi (2014). However, as supported by prior studies, when the magnitude of two-point correlation is sufficiently small, the confinement effect of the computational domain is insignificant, especially for one-point statistics (O'Neill *et al.* 2004; Lozano-Durán & Jiménez 2014; Lee & Moser 2015). Comparison of one-point statistics of turbulent kinetic energy, production and

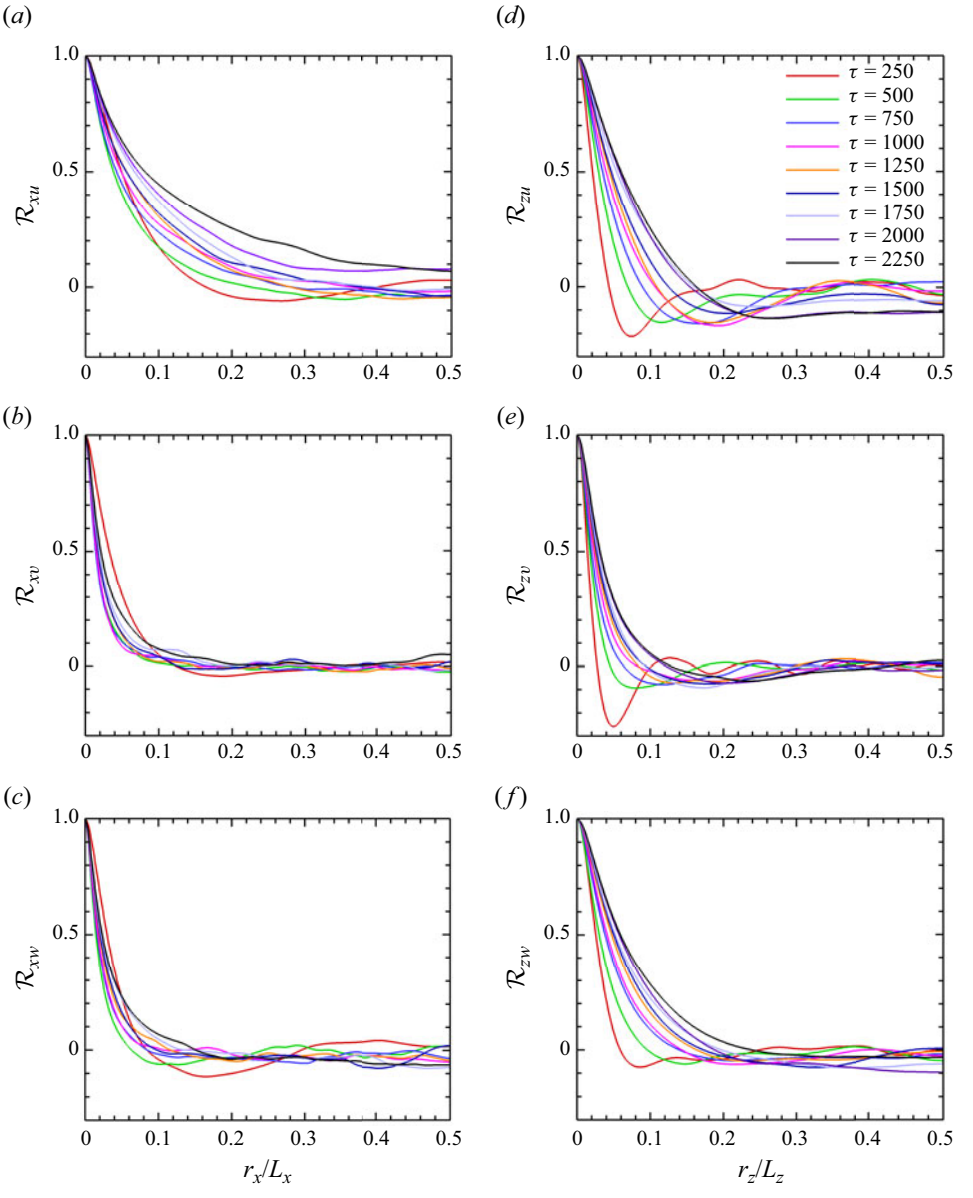

Figure 21. (*a–c*) Streamwise and (*d–f*) spanwise two-point correlations of (*a*,*d*) streamwise, (*b*,*e*) vertical and (*c*,*f*) spanwise velocities at the centreline at several time instants from $\tau = 250$ to $\tau = 2250$ for the case with $M_c = 1.8$.

dissipation terms with different τ_f at $M_c = 1.8$ are shown in figure 22. The good agreement of the results with $\tau_f = 1750$ and $\tau_f = 2250$ suggests that the data beyond $\tau_f = 1750$ still accurately captures the physical processes involved. Even for the pressure-dilatation term, which is relatively sensitive to the sample size, the results with $\tau_f = 1750$ and $\tau_f = 2250$ are very similar, except for noticeable differences near the edges of the mixing layer, as shown in figure 22(*f*). Additionally, we compared the two-dimensional conditionally averaged streamwise velocity, production and dissipation terms at $\tau_f = 1750$ and $\tau_f =$

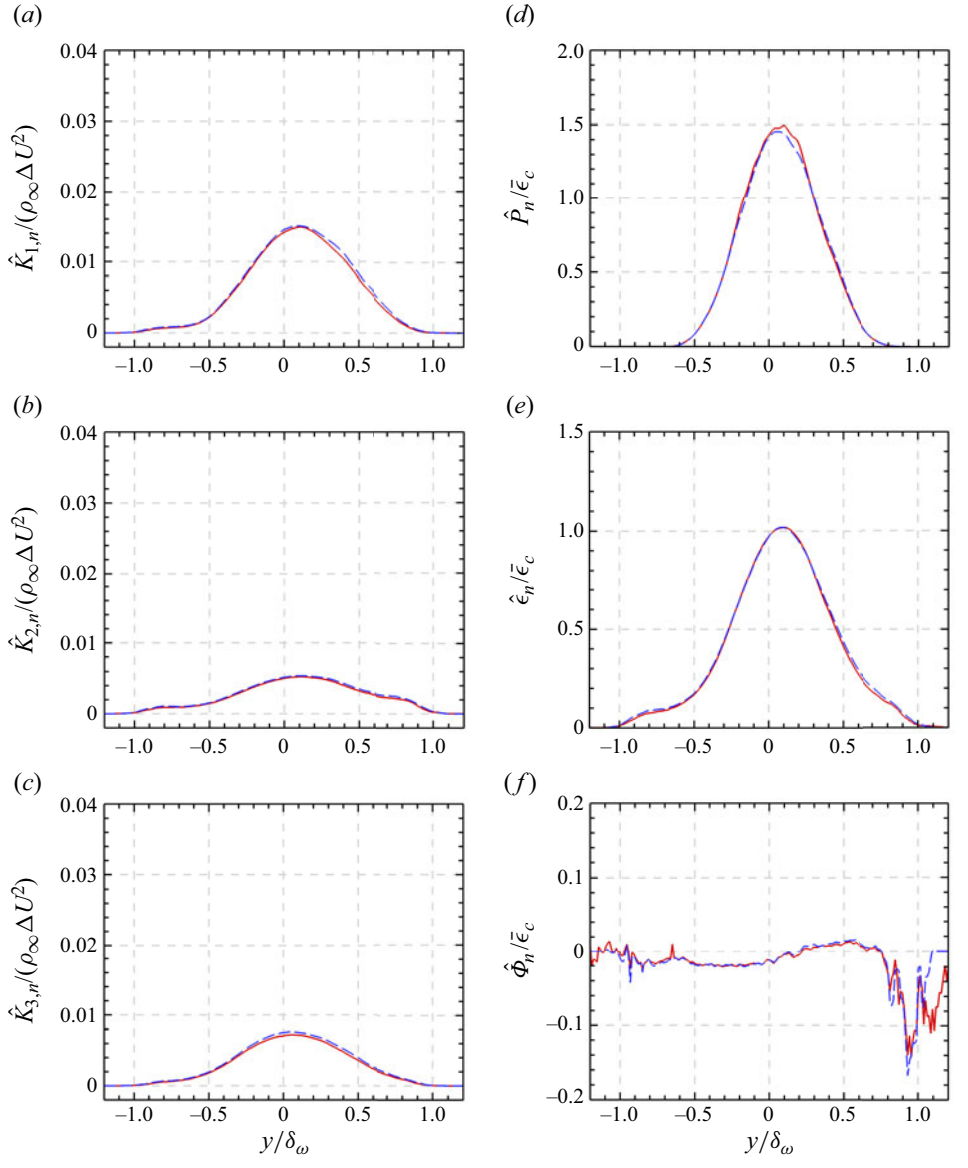

Figure 22. Comparison of one-point statistics with different τ_f for $M_c = 1.8$. (*a–c*) Conditionally averaged turbulent kinetic energy $\hat{K}_{i,n}/(\rho_\infty \Delta U^2)$. (*d–f*) Conditionally averaged production $\hat{P}_n/\bar{\epsilon}_c$, dissipation $\hat{\epsilon}_n/\bar{\epsilon}_c$ and pressure-dilatation $\hat{\Phi}_n/\bar{\epsilon}_c$.

2250 in figure 23 for $M_c = 1.8$. The results show that the differences between the two cases are minimal, occurring only in regions farther from the origin.

Table 2 contains the most relevant publications of DNS of temporally developing compressible mixing layer, together with M_c, the range of the self-similar period, the computational domain dimensions and the integral lengths. We can see that the largest integral length scale of $l_x/L_x = 0.151$ is obtained at the end of the self-similar region at $M_c = 1.8$ in the present work, and it is comparable to the previous numerical results of Vaghefi (2014) and Yu & Lu (2020).

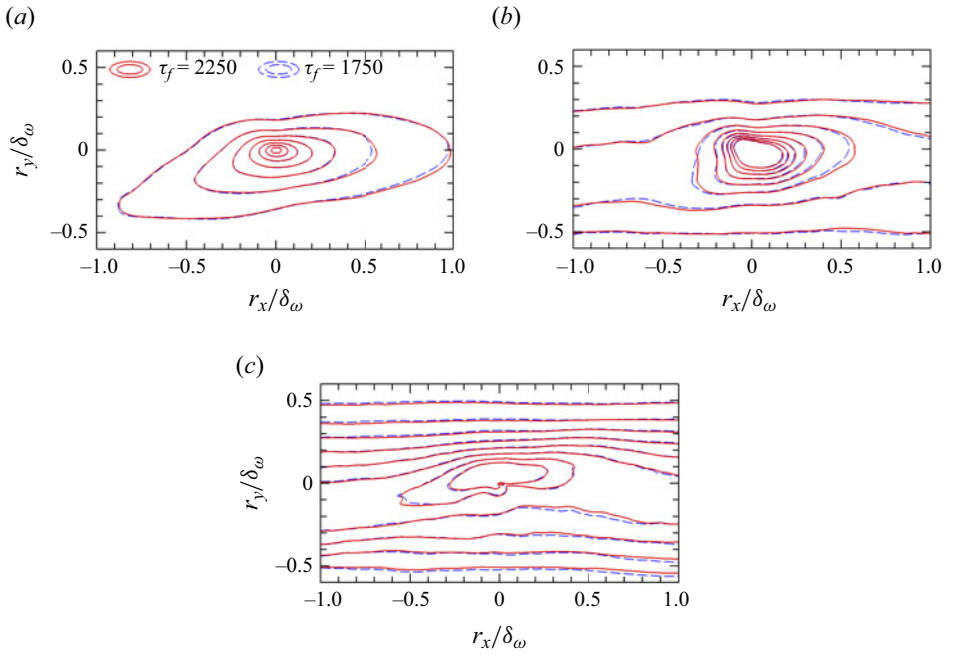

Figure 23. Comparison of two-dimensional conditionally averaged (*a*) streamwise velocity $\breve{u}_n/\Delta U$, (*b*) production $\breve{P}_n/\bar{\epsilon}_c$ and dissipation $\breve{\epsilon}_{1,n}/\bar{\epsilon}_c$ with different τ_f for $M_c = 1.8$.

Work	M_c	τ	L_x/δ_θ^0	L_y/δ_θ^0	L_z/δ_θ^0	l_x/L_x	l_z/L_z
Pantano & Sarkar (2002)	1.1	—	345	172	86	0.030	0.028
Vaghefi (2014)	1.8	$\tau_0 = 1300$	300	250	100	0.136	0.071
		$\tau_f = 1900$					
Arun *et al.* (2019)	1.2	—	314	157	78	0.076	—
		—					
Yu & Lu (2020)	1.6	$\tau_0 = 1002$	345	172	172	0.121	0.072
		$\tau_f = 1200$					
Vadrot, Giauque & Corre (2021)	1.1	$\tau_0 = 1700$	344	172	86	0.070	0.060
		$\tau_f = 2250$				0.120	0.080
Present work	1.8	$\tau_0 = 1250$	314	314	157	0.090	0.036
		$\tau_f = 2250$				0.151	0.043

Table 2. The beginning ($\tau = \tau_0$) and end ($\tau = \tau_f$) times of the self-similar period, domain lengths (L_x, L_y and L_z) and integral lengths (l_x and l_z) in the most relevant publications of DNS of temporally developing compressible mixing layer at higher convective Mach number. Only the integral lengths at the end time ($\tau = \tau_f$) of the self-similar period are presented by Pantano & Sarkar (2002), Vaghefi (2014), Arun *et al.* (2019) and Yu & Lu (2020).

We conclude from these results that the scale of the computational domain in this study is appropriate, and setting the end time of the self-similar period at $\tau_f = 2250$ for $M_c = 1.8$ is reasonable. The confinement effect of the computational domain is insignificant even though the two-point correlations do not exhibit complete decay to zero decorrelation within the computational domain.

References

ADRIAN, R.J., MEINHART, C.D. & TONKINS, C.D. 2000 Vortex organization in the outer region of the turbulent boundary layer. *J. Fluid Mech.* **422**, 1–54.

AGOSTINI, L. & LESCHZINER, M.A. 2014 On the influence of outer large-scale structures on near-wall turbulence in channel flow. *Phys. Fluids* **26** (7), 075107.

ARUN, S., SAMEEN, A., SRINIVASAN, B. & GIRIMAJI, S.S. 2019 Topology-based characterization of compressibility effects in mixing layers. *J. Fluid Mech.* **874**, 38–75.

ARUN, S., SAMEEN, A., SRINIVASAN, B. & GIRIMAJI, S.S. 2021 Scale-space energy density function transport equation for compressible inhomogeneous turbulent flows. *J. Fluid Mech.* **920**, A31.

BALSARA, D.S. & SHU, C.W. 2000 Monotonicity preserving weighted essentially non-oscillatory schemes with increasingly high order of accuracy. *J. Comput. Phys.* **160** (2), 405–452.

BALTZER, J.R., ADRIAN, R.J. & WU, X. 2013 Structural organization of large and very large scales in turbulent pipe flow simulation. *J. Fluid Mech.* **720**, 236–279.

BANDYOPADHYAY, P.R. & HUSSAIN, A.K.M.F. 1984 The coupling between scales in shear flows. *Phys. Fluids* **27** (9), 2221–2228.

BOLOTNOV, I.A., LAHEY, R.T., DREW, D.A., JANSEN, K.E. & OBERAI, A.A. 2010 Spectral analysis of turbulence based on the DNS of a channel flow. *Comput. Fluids* **39** (4), 640–655.

BROSS, M., SCHARNOWSKI, S. & KÄHLER, C.J. 2021 Large-scale coherent structures in compressible turbulent boundary layers. *J. Fluid Mech.* **911**, A2.

CHAN, C.I. & CHIN, R.C. 2022 Investigation of the influence of miniature vortex generators on the large-scale motions of a turbulent boundary layer. *J. Fluid Mech.* **932**, A29.

DE SILVA, C.M., PHILIP, J., HUTCHINS, N. & MARUSIC, I. 2017 Interfaces of uniform momentum zones in turbulent boundary layers. *J. Fluid Mech.* **820**, 451–478.

DENG, S., PAN, C., WANG, J. & HE, G. 2018 On the spatial organization of hairpin packets in a turbulent boundary layer at low-to-moderate Reynolds number. *J. Fluid Mech.* **844**, 635–668.

DENNIS, D.J.C. & NICKELS, T.B. 2011 Experimental measurement of large-scale three-dimensional structures in a turbulent boundary layer. Part 2. Long structures. *J. Fluid Mech.* **673**, 218–244.

DOMARADZKI, J.A., LIU, W., HÄRTEL, C. & KLEISER, L. 1994 Energy transfer in numerically simulated wall-bounded turbulent flows. *Phys. Fluids* **6** (4), 1583–1599.

EISMA, J., WESTERWEEL, J., OOMS, G. & ELSINGA, G.E. 2015 Interfaces and internal layers in a turbulent boundary layer. *Phys. Fluids* **27** (5), 055103.

FAN, D., XU, J., YAO, M.X. & HICKEY, J.-P. 2019 On the detection of internal interfacial layers in turbulent flows. *J. Fluid Mech.* **872**, 198–217.

FAN, Y. & LI, W. 2023 Spectral analysis of turbulence kinetic and internal energy budgets in hypersonic turbulent boundary layers. *Phys. Rev. Fluids* **8** (4), 044604.

FISCALETTI, D., GANAPATHISUBRAMANI, B. & ELSINGA, G.E. 2015 Amplitude and frequency modulation of the small scales in a jet. *J. Fluid Mech.* **772**, 756–783.

GANAPATHISUBRAMANI, B., HUTCHINS, N., HAMBLETON, W.T., LONGMIRE, E.K. & MARUSIC, I. 2005 Investigation of large-scale coherence in a turbulent boundary layer using two-point correlations. *J. Fluid Mech.* **524**, 57–80.

HUTCHINS, N. & MARUSIC, I. 2007 Evidence of very long meandering features in the logarithmic region of turbulent boundary layers. *J. Fluid Mech.* **579**, 1–28.

INOUE, M., MATHIS, R., MARUSIC, I. & PULLIN, D.I. 2012 Inner-layer intensities for the flat-plate turbulent boundary layer combining a predictive wall-model with large-eddy simulations. *Phys. Fluids* **24** (7), 075102.

JAHANBAKHSHI, R. & MADNIA, C.K. 2016 Entrainment in a compressible turbulent shear layer. *J. Fluid Mech.* **797** (2016), 564–603.

JIMÉNEZ, J. 2018 Coherent structures in wall-bounded turbulence. *J. Fluid Mech.* **842**, P1.

KAWATA, T. & TSUKAHARA, T. 2022 Spectral analysis on transport budgets of turbulent heat fluxes in plane Couette turbulence. *Energies* **15** (14), 1–27.

KIM, K.C. & ADRIAN, R.J. 1999 Very large-scale motion in the outer layer. *Phys. Fluids* **11** (2), 417–422.

KLEIN, M., SADIKI, A. & JANICKA, J. 2003 A digital filter based generation of inflow data for spatially developing direct numerical or large eddy simulations. *J. Comput. Phys.* **186** (2), 652–665.

KRUG, D., HOLZNER, M., LÜTHI, B., WOLF, M., KINZELBACH, W. & TSINOBER, A. 2015 The turbulent/non-turbulent interface in an inclined dense gravity current. *J. Fluid Mech.* **765**, 303–324.

LEE, J., AHN, J. & SUNG, H.J. 2015 Comparison of large- and very-large-scale motions in turbulent pipe and channel flows. *Phys. Fluids* **27** (2), 025101.

LEE, J., LEE, J.H., CHOI, J.-I. & SUNG, H.J. 2014 Spatial organization of large- and very-large-scale motions in a turbulent channel flow. *J. Fluid Mech.* **749**, 818–840.

LEE, M. & MOSER, R.D. 2015 Direct numerical simulation of turbulent channel flow up to $Re_\tau = 5200$. *J. Fluid Mech.* **774**, 395–415.

LEE, M. & MOSER, R.D. 2019 Spectral analysis of the budget equation in turbulent channel flows at high Reynolds number. *J. Fluid Mech.* **860**, 886–938.

LELE, S.K. 1992 Compact finite difference schemes with spectral-like resolution. *J. Comput. Phys.* **103** (1), 16–42.

LI, D., PEYVAN, A., GHIASI, Z., KOMPERDA, J. & MASHAYEK, F. 2021 Compressibility effects on energy exchange mechanisms in a spatially developing plane free shear layer. *J. Fluid Mech.* **910**, A9.

LIU, H., WANG, G. & ZHENG, X. 2019 Amplitude modulation between multi-scale turbulent motions in high-Reynolds-number atmospheric surface layers. *J. Fluid Mech.* **861**, 585–607.

LOZANO-DURÁN, A. & JIMÉNEZ, J. 2014 Effect of the computational domain on direct simulations of turbulent channels up to $Re_\tau = 4200$. *Phys. Fluids* **26** (1), 011702.

LUMLEY, J.L. 1964 Spectral energy budget in wall turbulence. *Phys. Fluids* **7** (2), 190–196.

MAHLE, I. 2007 Direct and large-eddy simulation of inert and reacting compressible turbulent shear layers. PhD thesis, Technische Universität München, Germany.

MARUSIC, I., MATHIS, R. & HUTCHINS, N. 2010 Predictive model for wall-bounded turbulent flow. *Science* **329** (5988), 193–196.

MATHIS, R., HUTCHINS, N. & MARUSIC, I. 2009 Large-scale amplitude modulation of the small-scale structures in turbulent boundary layers. *J. Fluid Mech.* **628**, 311–337.

MATHIS, R., HUTCHINS, N. & MARUSIC, I. 2011*a* A predictive inner–outer model for streamwise turbulence statistics in wall-bounded flows. *J. Fluid Mech.* **681**, 537–566.

MATHIS, R., MARUSIC, I., HUTCHINS, N. & SREENIVASAN, K.R. 2011*b* The relationship between the velocity skewness and the amplitude modulation of the small scale by the large scale in turbulent boundary layers. *Phys. Fluids* **23** (12), 121702.

MESSERSMITH, N.L. & DUTTON, J.C. 1996 Characteristic features of large structures in compressible mixing layers. *AIAA J.* **34** (9), 1814–1821.

MIZUNO, Y. 2016 Spectra of energy transport in turbulent channel flows for moderate Reynolds numbers. *J. Fluid Mech.* **805**, 171–187.

MONTY, J.P., HUTCHINS, N., NG, H.C.H., MARUSIC, I. & CHONG, M.S. 2009 A comparison of turbulent pipe, channel and boundary layer flows. *J. Fluid Mech.* **632**, 431–442.

MONTY, J.P., STEWART, J.A., WILLIAMS, R.C. & CHONG, M.S. 2007 Large-scale features in turbulent pipe and channel flows. *J. Fluid Mech.* **589**, 147–156.

NEKKANTI, A., NIDHAN, S., SCHMIDT, O.T. & SARKAR, S. 2023 Large-scale streaks in a turbulent bluff body wake. *J. Fluid Mech.* **974**, A47.

NOGUEIRA, P.A.S., CAVALIERI, A.V.G., JORDAN, P. & JAUNET, V. 2019 Large-scale streaky structures in turbulent jets. *J. Fluid Mech.* **873**, 211–237.

O'NEILL, P., NICOLAIDES, D., HONNERY, D.R. & SORIA, J. 2004 Autocorrelation functions and the determination of integral length with reference to experimental and numerical data. In *Proceedings of the Fifteenth Australasian Fluid Mechanics Conference* (ed. M. Behnia, W. Lin & G.D. McBain), pp. 1–4. University of Sydney.

PANTANO, C. & SARKAR, S. 2002 A study of compressibility effects in the high-speed turbulent shear layer using direct simulation. *J. Fluid Mech.* **451**, 329–371.

PHILIP, J., MENEVEAU, C., DE SILVA, C.M. & MARUSIC, I. 2014 Multiscale analysis of fluxes at the turbulent/non-turbulent interface in high Reynolds number boundary layers. *Phys. Fluids* **26** (1), 015105.

PIROZZOLI, S. & BERNARDINI, M. 2011 Turbulence in supersonic boundary layers at moderate Reynolds number. *J. Fluid Mech.* **688**, 120–168.

PIROZZOLI, S., BERNARDINI, M., MARIÉ, S. & GRASSO, F. 2015 Early evolution of the compressible mixing layer issued from two turbulent streams. *J. Fluid Mech.* **777**, 196–218.

POPE, S.B. 2000 *Turbulent Flows*. Cambridge University Press.

RAGAB, S.A. & WU, J.L. 1989 Linear instabilities in two-dimensional compressible mixing layers. *Phys. Fluids* A **1** (6), 957–966.

RECKINGER, S.J., LIVESCU, D. & VASILYEV, O.V. 2016 Comprehensive numerical methodology for direct numerical simulations of compressible Rayleigh–Taylor instability. *J. Comput. Phys.* **313**, 181–208.

REUTHER, N. & KÄHLER, C.J. 2020 Effect of the intermittency dynamics on single and multipoint statistics of turbulent boundary layers. *J. Fluid Mech.* **897**, A11.

ROGERS, M.M. & MOSER, R.D. 1994 Direct simulation of a self-similar turbulent mixing layer. *Phys. Fluids* **6** (2), 903–923.

ROSSMANN, T., MUNGAL, M.G. & HANSON, R.K. 2002 Evolution and growth of large-scale structures in high compressibility mixing layers. *J. Turbul.* **3**, 27–29.

SAMIE, M., APARECE-SCUTARIU, V., LAVOIE, P., SHIN, D.-H. & POLLARD, A. 2022 Three-dimensional large-scale and very-large-scale coherent structures in a turbulent axisymmetric jet. *J. Fluid Mech.* **948**, A29.

SAMIE, M., LAVOIE, P. & POLLARD, A. 2021 Quantifying eddy structures and very-large-scale motions in turbulent round jets. *J. Fluid Mech.* **916**, A2.

SAMTANEY, R., PULLIN, D.I. & KOSOVIĆ, B. 2001 Direct numerical simulation of decaying compressible turbulence and shocklet statistics. *Phys. Fluids* **13** (5), 1415–1430.

SARKAR, S. 1995 The stabilizing effect of compressibility in turbulent shear flow. *J. Fluid Mech.* **282**, 163–186.

DA SILVA, C.B., HUNT, J.C.R., EAMES, I. & WESTERWEEL, J. 2014 Interfacial layers between regions of different turbulence intensity. *Annu. Rev. Fluid Mech.* **46** (1), 567–590.

SMITS, A.J., MCKEON, B.J. & MARUSIC, I. 2011 High–Reynolds number wall turbulence. *Annu. Rev. Fluid Mech.* **43** (1), 353–375.

SUTHERLAND, W. 1893 LII. The viscosity of gases and molecular force. *Lond. Edinb. Dub. Phil. Mag. J. Sci.* **36** (223), 507–531.

TALLURU, K.M., BAIDYA, R., HUTCHINS, N. & MARUSIC, I. 2014 Amplitude modulation of all three velocity components in turbulent boundary layers. *J. Fluid Mech.* **746**, R1.

TOWNSEND, A.A.R. 1976 *The Structure of Turbulent Shear Flow*. Cambridge University Press.

VADROT, A., GIAUQUE, A. & CORRE, C. 2021 Direct numerical simulations of temporal compressible mixing layers in a Bethe–Zel'dovich–Thompson dense gas: influence of the convective Mach number. *J. Fluid Mech.* **922**, A5.

VAGHEFI, N.S. 2014 Simulation and modeling of compressible turbulent mixing layer. PhD thesis, State University of New York, New York, USA.

VAGHEFI, N.S. & MADNIA, C.K. 2015 Local flow topology and velocity gradient invariants in compressible turbulent mixing layer. *J. Fluid Mech.* **774**, 67–94.

VREMAN, A.W., SANDHAM, N.D. & LUO, K.H. 1996 Compressible mixing layer growth rate and turbulence characteristics. *J. Fluid Mech.* **320**, 235–258.

WALLACE, J.M. 2016 Quadrant analysis in turbulence research: history and evolution. *Annu. Rev. Fluid Mech.* **48** (1), 131–158.

WANG, G. & ZHENG, X. 2016 Very large scale motions in the atmospheric surface layer: a field investigation. *J. Fluid Mech.* **802**, 464–489.

WANG, J., SHI, Y., WANG, L.-P., XIAO, Z., HE, X.T. & CHEN, S. 2012 Effect of compressibility on the small-scale structures in isotropic turbulence. *J. Fluid Mech.* **713**, 588–631.

WANG, J., WANG, L., XIAO, Z., SHI, Y. & CHEN, S. 2010 A hybrid numerical simulation of isotropic compressible turbulence. *J. Comput. Phys.* **229** (13), 5257–5279.

WANG, X., GUO, J., WANG, J. & CHEN, S. 2024 Interfaces of high- and low-speed large-scale structures in compressible turbulent mixing layers: compressibility effects and structures. *J. Fluid Mech.* **981**, A6.

WANG, X., WANG, J. & CHEN, S. 2022 Compressibility effects on statistics and coherent structures of compressible turbulent mixing layers. *J. Fluid Mech.* **947**, A38.

WANG, X., WANG, J., LI, H. & CHEN, S. 2021 Kinetic energy transfer in compressible homogeneous anisotropic turbulence. *Phys. Rev. Fluids* **6** (6), 064601.

WATANABE, T. & NAGATA, K. 2021 Large-scale characteristics of a stably stratified turbulent shear layer. *J. Fluid. Mech.* **927**, A27.

WATANABE, T., RILEY, J.J., NAGATA, K., MATSUDA, K. & ONISHI, R. 2019 Hairpin vortices and highly elongated flow structures in a stably stratified shear layer. *J. Fluid Mech.* **878**, 37–61.

WATANABE, T., ZHANG, X. & NAGATA, K. 2018 Turbulent/non-turbulent interfaces detected in DNS of incompressible turbulent boundary layers. *Phys. Fluids* **30** (3), 035102.

WESTERWEEL, J., FUKUSHIMA, C., PEDERSEN, J.M. & HUNT, J.C.R. 2005 Mechanics of the turbulent-nonturbulent interface of a jet. *Phys. Rev. Lett.* **95** (17), 174501.

YU, J.-L. & LU, X.-Y. 2020 Subgrid effects on the filtered velocity gradient dynamics in compressible turbulence. *J. Fluid Mech.* **892**, A24.

YU, M. & XU, C. 2022 Predictive models for near-wall velocity and temperature fluctuations in supersonic wall-bounded turbulence. *J. Fluid Mech.* **937**, A32.

ZHOU, Q., HE, F. & SHEN, M.Y. 2012 Direct numerical simulation of a spatially developing compressible plane mixing layer: flow structures and mean flow properties. *J. Fluid Mech.* **711**, 437–468.